

AGU Advances

RESEARCH ARTICLE

10.1029/2023AV000979

Peer Review The peer review history for this article is available as a PDF in the Supporting Information.

Key Points:

- We present the first 3D linked models of dynamic earthquake rupture and long-term slow slip cycles along the flat-slab Cocos plate
- The modeled long-term slow slip cycles and earthquake dynamic rupture capture key observations on timescales from decades to seconds
- The transient stress evolution of the long-term slow slip cycles may have initiated the 2014 Mw 7.3 Guerrero, Mexico earthquake

Supporting Information:

Supporting Information may be found in the online version of this article.

Correspondence to:

D. Li,
d.li@lmu.de;
d.li@gns.cri.nz

Citation:

Li, D., & Gabriel, A.-A. (2024). Linking 3D long-term slow-slip cycle models with rupture dynamics: The nucleation of the 2014 M_w 7.3 Guerrero, Mexico earthquake. *AGU Advances*, 5, e2023AV000979. <https://doi.org/10.1029/2023AV000979>

Received 18 JUN 2023

Accepted 6 FEB 2024

Author Contributions:

Conceptualization: Duo Li, Alice-Agnes Gabriel
Formal analysis: Duo Li
Funding acquisition: Alice-Agnes Gabriel
Investigation: Duo Li
Methodology: Duo Li, Alice-Agnes Gabriel
Project administration: Duo Li
Resources: Alice-Agnes Gabriel
Software: Duo Li, Alice-Agnes Gabriel
Supervision: Alice-Agnes Gabriel

© 2024. The Authors.

This is an open access article under the terms of the [Creative Commons Attribution License](#), which permits use, distribution and reproduction in any medium, provided the original work is properly cited.

Linking 3D Long-Term Slow-Slip Cycle Models With Rupture Dynamics: The Nucleation of the 2014 M_w 7.3 Guerrero, Mexico Earthquake

Duo Li^{1,2}  and Alice-Agnes Gabriel^{1,3} 

¹Department of Earth and Environmental Sciences, Ludwig-Maximilians-Universität München, Munich, Germany, ²Now at GNS Science, Lower Hutt, New Zealand, ³Institute of Geophysics and Planetary Physics, Scripps Institution of Oceanography, University of California San Diego, La Jolla, CA, USA

Abstract Slow slip events (SSEs) have been observed in spatial and temporal proximity to megathrust earthquakes in various subduction zones, including the 2014 M_w 7.3 Guerrero, Mexico earthquake which was preceded by a M_w 7.6 SSE. However, the underlying physics connecting SSEs to earthquakes remains elusive. Here, we link 3D slow-slip cycle models with dynamic rupture simulations across the geometrically complex flat-slab Cocos plate boundary. Our physics-based models reproduce key regional geodetic and teleseismic fault slip observations on timescales from decades to seconds. We find that accelerating SSE fronts transiently increase shear stress at the down-dip end of the seismogenic zone, modulated by the complex geometry beneath the Guerrero segment. The shear stresses cast by the migrating fronts of the 2014 M_w 7.6 SSE are significantly larger than those during the three previous episodic SSEs that occurred along the same portion of the megathrust. We show that the SSE transient stresses are large enough to nucleate earthquake dynamic rupture and affect rupture dynamics. However, additional frictional asperities in the seismogenic part of the megathrust are required to explain the observed complexities in the coseismic energy release and static surface displacements of the Guerrero earthquake. We conclude that it is crucial to jointly analyze the long- and short-term interactions and complexities of SSEs and megathrust earthquakes across several (a)seismic cycles accounting for megathrust geometry. Our study has important implications for identifying earthquake precursors and understanding the link between transient and sudden megathrust faulting processes.

Plain Language Summary The 2014 M_w 7.3 Guerrero, Mexico earthquake was preceded by an M_w 7.6 slow slip event (SSE), a transient of aseismic fault slip, which offers a valuable opportunity to explore the relationship between slow slip and major subduction earthquakes. By modeling both long-term cycles of slow slip events and dynamic earthquake rupture, we reproduce various measurements from geodetic surveys and seismic recordings. We find that as the migrating front of the 2014 SSE accelerated, it caused additional loading at depth where the earthquake occurred. In this case, the stress levels of the preceding 2014 SSE were notably higher than previous SSEs which appeared in the same fault portion between 2001 and 2014, and may have contributed to initiating the earthquake. Additionally, we find that variations in friction across the megathrust affect the complexity of energy release and surface displacements during the earthquake. By examining the temporary and long-term interactions between SSEs and earthquakes, we gain important insights into potential earthquake precursors and the processes involved in how faults move. This research holds significant implications for enhancing our understanding of how large earthquakes occur in subduction zones.

1. Introduction

Transient slow deformation of faults, slow-slip events, or silent earthquakes have been observed at convergent plate boundaries (Douglas et al., 2005; Dragert et al., 2001; Peng & Gomberg, 2010; Schwartz & Rokosky, 2007; Shelly et al., 2006) and at large continental faults, for example, the San Andreas fault (Linde et al., 1996; Rousset et al., 2019). Slow slip events (SSEs) may be accompanied by low-frequency seismic radiation, including tectonic tremors, low-frequency earthquakes, and very-low-frequency earthquakes (Khoshmanesh et al., 2020; Shelly et al., 2007). SSEs usually slip 10–100 times faster than the tectonic loading and last from days to years at depths close to the brittle-ductile transition (Dragert et al., 2001; Peng & Gomberg, 2010; Schwartz & Rokosky, 2007). The physical mechanisms underlying SSEs and their interaction with earthquakes are debated (Bürgmann, 2018). The spatial viability of both fast and slow earthquakes on plate-boundary faults has been attributed to several

Validation: Duo Li**Visualization:** Duo Li**Writing – original draft:** Duo Li, Alice-Agnes Gabriel**Writing – review & editing:** Duo Li, Alice-Agnes Gabriel

factors, including structural and material heterogeneity (Lay et al., 2012; D. Li & Liu, 2016; Tobin & Saffer, 2009; Ulrich et al., 2022; Wang, 2010), rheological variability with depth (Gao & Wang, 2017; Saffer & Wallace, 2015) and fluid migration within oceanic sedimentary layers (W. B. Frank et al., 2015; Zhu et al., 2020).

Whether transient slow slip can serve as a universal precursor of eminent megathrust earthquake initiation is essential for seismic and tsunami hazard assessments in metropolitan margins (Bürgmann, 2018; Obara & Kato, 2016; Pritchard et al., 2020; Ruiz et al., 2014). However, the spatial and temporal interactions between slow and fast earthquakes, specifically the potential of slow-slip triggering megathrust earthquakes, remain enigmatic. Due to the observational challenges associated with the large variability of space and time scales, physics-based models are indispensable to illuminate the physics and in-situ fault properties, rendering SSE triggering of large earthquakes plausible.

On 18 April 2014, a M_w 7.3 megathrust earthquake struck the coast of Mexico at the western edge of the Guerrero Gap, which had experienced no significant seismic events since 1911 (Kostoglodov et al., 1996; Radiguet et al., 2012). Geodetic inversions suggest that long-term slow-slip cycles have accommodated most of the plate convergence on the sub-horizontal oceanic slab between 20 and 45 km depth in Guerrero (Kostoglodov et al., 1996; Radiguet et al., 2012, 2016) (Figure 1a). In addition to long-term SSEs, transient bursts of short-term low-frequency earthquakes and tectonic tremors have been detected at different depths along the slab (Husker et al., 2012; W. B. Frank et al., 2015; W. Frank et al., 2015; Pérez-Campos et al., 2008). Slow-slip and slow earthquakes have been attributed to the elevated pore fluid pressure associated with an ultra-low velocity layer atop the subducting plate derived from dense-array seismic imaging (Song et al., 2009). Recent off-shore seismic observations have revealed a combination of co-seismic earthquake, aseismic and creeping deformation, suggesting the existence of multiple asperities across the slab interface (Plata-Martinez et al., 2021). Considering the unique slip characteristics of the Guerrero Gap, the initiation of the 2014 M_w 7.3 earthquake has been related to the accumulated static Coulomb stress changes cast by an ongoing slow-slip event below 20 km depth that eventually accumulated an equivalent moment magnitude of M_w 7.6 on the megathrust interface (Radiguet et al., 2016; Gualandi et al., 2017).

Integrated modeling of long-term tectonic loading and coseismic rupture advances the understanding of the dynamics of interseismic and coseismic slip, as well as their interplay (Cattania, 2019; Kaneko et al., 2011; Liu et al., 2020). While a few implementations have been developed to integrate long-term slow interseismic loading and fast coseismic rupture (Cattania & Segall, 2021; Segall et al., 2010; Yang & Dunham, 2023), they typically omit inertia effects during the interseismic period. Liu et al. (2020) couple two 3D finite element methods, one for long-term seismic cycle modeling and another for short-term dynamic earthquake rupture, linking stress and frictional parameters in geometrically simple setups. Cattania and Segall (2021) use 1D fractally rough faults and heterogeneous effective normal stress to model the spatiotemporal relationships between precursory slow slip and clusters of foreshocks. Due to algorithmic complexity and computational cost (e.g., Jiang et al., 2022; Lapusta & Liu, 2009; Thomas et al., 2014; Uphoff et al., 2023), it remains challenging to model the complete dynamics of 3D seismic cycles using a single code for a heterogeneous, geometrically complex subduction zone (see Text S1 in Supporting Information S1). Such modeling should also allow for observational data validation, as we undertake here.

In this study, we present 3D numerical models of the dynamic rupture of the 2014 M_w 7.3 Guerrero earthquake, linked to 3D episodic slow-slip cycles under long-term tectonic loading, ensuring consistent stress states across the fault interface. Physics-based models of earthquake initiation, propagation, and arrest require choices regarding the pre-existing state of stress and fault strength governing frictional sliding (Harris et al., 2021; Oglesby & Mai, 2012; Ramos et al., 2021; van Zelst et al., 2019). Our SSE cycle and dynamic rupture models account for the same geophysical and geological observational inferences, such as the regional slab geometry, elevated pore fluid pressure, and depth-dependent frictional strength constrained from laboratory experiments and thermal modeling (Section 2). We bridge time scales from decades governing four episodes of long-term SSEs to fractions of seconds during earthquake rupture within the Guerrero Gap using the SSE cycle results to inform the dynamic earthquake rupture scenario models. The modeled, observationally constrained, transient stress evolution of the 2014 SSE event can lead to spontaneous co-seismic failure in the hypocentral region of the Guerrero earthquake. However, the episodic non-linear variability in shear stress caused by the three preceding SSEs, which correspond to the 2002, 2006, and 2009–2010 SSEs, remains too small compared to the high static fault strength required to match observations in the dynamic rupture model (Section 3). We also find that, in addition to

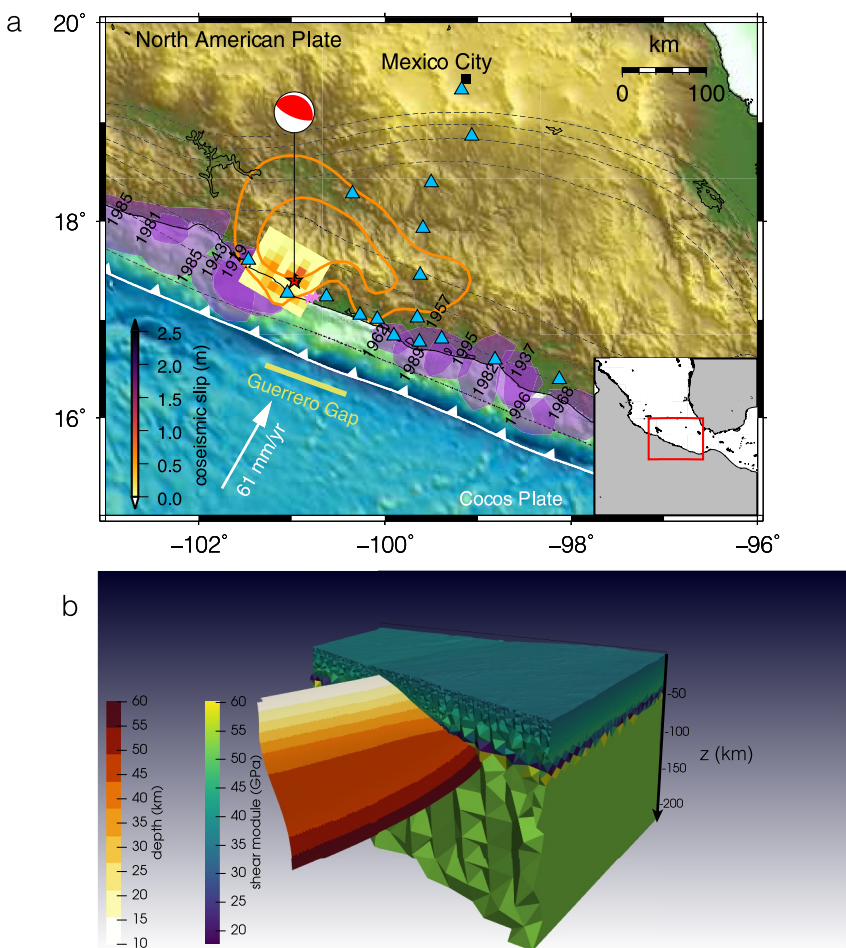


Figure 1. (a) Map of central Mexico where the Cocos plate subducts beneath the North American plate at a rate of 61 mm/yr (Relative Motion Model, DeMets et al., 2010). The so-called Guerrero Seismic Gap is a 100-km long segment between 100.2°W and 101.2°W (yellow bar) that lacks recent large earthquakes (Lowry et al., 2001). Purple shades indicate large ($M_w \leq 6.8$) earthquakes after 1940 (Lowry et al., 2001). The focal mechanism of the 2014 M_w 7.3 Guerrero earthquake is shown in red (strike:304°, dip:21°, rake:99°, Global Centroid Moment Tensor catalog (GCMT) (Dziewonski et al., 1981; Ekström et al., 2012)). A finite coseismic source model using teleseismic inversion is shown as yellow-to-red-to-black rectangles (Ye et al., 2016). The orange contours indicate the 10 and 20 cm aseismic levels of fault slip during the 2014 M_w 7.3 slow-slip events (Radiguet et al., 2016). The blue triangles mark the permanent Global Positioning System stations used in a geodetic inversion of both the coseismic and slow slip (Gualandi et al., 2017). Depth contours from 5 km depth (trench) to 80 km depth are shown as dashed lines with 5 km depth spacing. Mexico City is shown in black. (b) Slab surface geometry extending from the trench to a depth of 60 km in both slow-slip cycle and dynamic rupture simulations. This slab geometry is inferred from the Middle America Seismic Experiment (MASE) (Pérez-Campos et al., 2008). We use the standard global projection WGS84/UTM, zone 11N to Cartesian coordinates. The detailed description of mesh generation and convergence analysis can be found in Text S2 in Supporting Information S1. Tetrahedral elements are color-coded by a 1D layered velocity model from seismic imaging (Dougherty & Clayton, 2014) that is used in the dynamic rupture model.

SSE-induced stress heterogeneity, the complex propagation and arrest of the Guerrero earthquake require pre-existing variable friction properties. Our study provides a mechanically self-consistent model for slow-slip triggered megathrust earthquakes and has important implications for the interaction between earthquakes and slow-slip in subduction zones and at large continental faults worldwide (Section 4).

2. Methods

We model episodic slow-slip cycles spontaneously emerging under long-term geological loading along the curved slab interface of the Guerrero Gap (Section 2.1). The long-term tectonic loading, which accumulates fault shear stresses, is balanced by the fault strength which is defined from a laboratory-derived rate-and-state friction

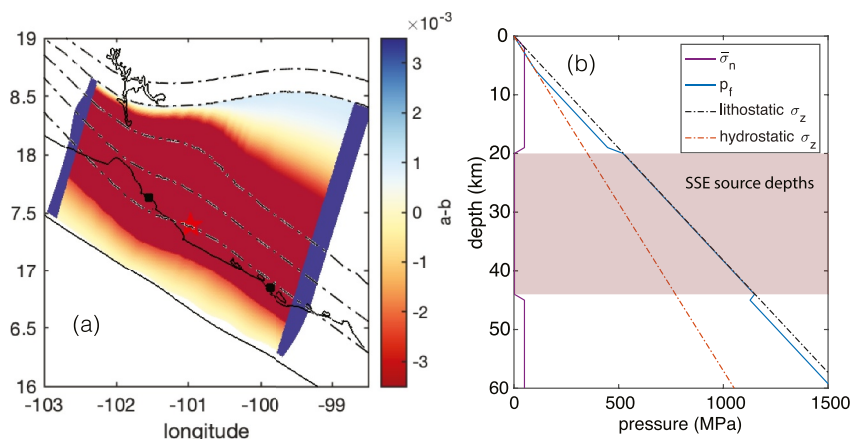


Figure 2. (a) Map view of the dimensionless frictional parameter $a - b$ on the fault. The distribution of $(a - b)$ at different temperatures was obtained from laboratory experiments on wet gabbro gouges (He et al., 2007). We project this temperature-dependent $(a - b)$ distribution onto the slab interface using the thermal profile from a 2D steady-state thermal model constrained by P-wave seismic tomography in central Mexico. The transition where $a - b = 0$ occurs at a depth of 42 km. (b) Along-depth profile of effective normal stress $\bar{\sigma}_n$ and pore fluid pressure p_f used in both the Slow slip event cycle and dynamic rupture models, and hydrostatic and lithostatic pressures σ_z as references.

law (Section 2.1.2). We constrain the fault frictional parameters by combining laboratory experiments on wet gabbro gouges (He et al., 2007) with a 2D steady-state thermal model constrained by P-wave seismic tomography (Manea & Manea, 2011). We extend a previous model that focused on the deeper part (10–60 km depth) of the slab covering episodic SSEs only (Perez-Silva et al., 2021). Here, we consider the geometrically complex slab up to the trench and thus include the entire seismogenic zone (5–60 km depth). We account for elevated pore fluid pressure atop the oceanic plate which locally reduces fault strength and eventually leads to episodic slow-slip emerging between depths of 20 and 45 km (Section 2.1.1, Figure 2). This elevation of pore fluid pressure has been suggested based on the seismically inferred high V_p/V_s ratios in central Mexico (Song et al., 2009) as well as in other subduction zones (Audet et al., 2009; Shelly et al., 2006).

2.1. 3D Quasi-Dynamic Simulations of the Long-Term Slow-Slip Cycles

Direct observations of slow-slip cycles are limited, motivating numerical simulations to elucidate the underlying mechanics of SSE and earthquake interactions. We simulate long-term slow-slip sequences on a convergent plate boundary and analyze the time-dependent evolution of slip rates and shear stresses on the fault interface in 3D (Figure 1b). We use a quasi-dynamic formulation and the Boundary Element Method. Our forward model adopts a laboratory-derived rate-and-state friction law and a 3D realistic subducting slab geometry beneath central Mexico. The governing equations relate the temporal shear stress evolution of an individual element in response to fault slip and long-term plate convergence following Rice (1993) as

$$\tau_i(t) = - \sum_{j=1}^N K_{i,j} (\delta_j(t) - V_{pl}t) - \eta \frac{d\delta_i(t)}{dt}, \quad (1)$$

where $\delta_i(t)$ is the fault slip and $K_{i,j}$ is the shear stress in element j due to a unit dislocation in dip direction of element i . The static Green's function $K_{i,j}$ is calculated using triangular dislocations in a uniform half-space (Stuart et al., 1997) assuming a homogeneous shear modulus of $\mu = 30$ GPa and density $\rho = 2,670$ kg/m³. The plate convergent rate V_{pl} is set to be uniformly 61 mm/year based on a global plate motion model, the Relative Motion Model (DeMets et al., 2010).

We use the open-source code TriBIE (<https://github.com/daisy20170101/TriBIE>) (D. Li & Liu, 2016; Perez-Silva et al., 2021), which is parallelized with OpenMPI and has been verified in 2D and 3D community benchmark exercises (Erickson et al., 2023; Jiang et al., 2022). We here use the quasi-dynamic approach approximating inertia effects with radiation damping for our SSE cycle simulations. To this end, the radiation damping factor $\eta = \mu/(2c_s)$ (with c_s being the shear wave speed) has been introduced (Rice, 1993). Compared to fully dynamic

simulations, the quasi-dynamic approach can lead to similar overall seismic cycle behavior but differing rupture dynamics (Jiang et al., 2022; Lapusta & Liu, 2009; Thomas et al., 2014). We detail all slow-slip cycle modeling parameters in the following.

2.1.1. Effective Normal Stress

Figure 2b shows the along-depth profiles of our assumed effective normal stress $\bar{\sigma}_n$, pore fluid pressure (p_f), hydrostatic ($0.37\sigma_z$) and lithostatic pressures (σ_z). We assume that lithostatic pressure is depth-dependent with a constant overburden gradient (i.e., $\sigma_z = \rho g (-z)$). The effective normal stress, defined as the difference between lithostatic pressure and pore fluid pressure, increases with depth at a constant gradient $\bar{\sigma}_n = 28 \text{ MPa/km}$ until a depth of 2.7 km. At lower depths, effective normal stress remains constant as $\bar{\sigma}_n = 50 \text{ MPa}$ except at the SSE source depth between 20 and 45 km. An effective normal stress of 50 MPa at seismogenic depth is a common assumption used in community benchmark studies (Jiang et al., 2022).

To reproduce the relatively low stress drops inferred for SSEs, we assume a low effective normal stress of $\bar{\sigma}_n^{\text{SSE}} = 2.5 \text{ MPa}$ at depths between 20 and 45 km based on our previous work for a narrower slab geometry (Perez-Silva et al., 2021) and linked to elevated pore fluid pressure. Such high, near-lithostatic pore fluid pressure is supported by the observed elevated ratio between V_p and V_s from seismic imaging along the coast of southwest Japan, Cascadia, and central Mexico (Audet & Burgmann, 2014; Song et al., 2009).

2.1.2. Rate-And-State Friction

Fault shear strength in the quasi-dynamic SSE simulation is governed by a laboratory-derived rate and state-dependent friction law, the aging law (Dieterich, 1979; Ruina, 1983). The effective friction coefficient f depends on the fault slip rate v and a single state variable θ as

$$\tau = \bar{\sigma}_n f = (\sigma_n - p) \left[f_0 + a \ln\left(\frac{v}{v_0}\right) + b \ln\left(\frac{v_0 \theta}{D_{RS}}\right) \right]. \quad (2)$$

Here, a and b are non-dimensional friction parameters for the direct effect and evolution effect, respectively, D_{RS} is the characteristic slip distance over which θ evolves in response to velocity steps, f_0 is the friction coefficient at a reference velocity v_0 at steady state, and $\bar{\sigma}_n = \sigma_n - p_f$ is the effective normal stress, defined as lithostatic loading stress minus the pore fluid pressure.

At steady state $\theta = D_{RS}/v$, the friction coefficient is $f_s = f_0 + (a - b) \ln\left(\frac{v}{v_0}\right)$. Slip remains stable, and any slip perturbation evolves toward a steady state when the friction stability parameter $(a - b)$ is positive (velocity-strengthening, VS). Slip can be either unstable or conditionally stable when $(a - b)$ is negative (velocity-weakening, VW). We use uniform distributions for the initial slip rate V_{ini} and the initial state variable θ_{ini} on the entire fault.

We adopt the definition of the critical nucleation length h_{RA}^* based on the fracture energy balance for a quasi-statically expanding crack (Rubin & Ampuero, 2005),

$$h_{RA}^* = \frac{2\mu b D_{RS}}{\pi(1-\nu)(b-a)^2 \bar{\sigma}}. \quad (3)$$

Here, we assume a shear modulus of $\mu = 30 \text{ GPa}$ and Poisson's ratio of $\nu = 0.25$. The ratio between the maximum width of the velocity-weakening portion of the slab and the critical nucleation length (h_{RA}^*) significantly affects the slip behavior of modeled SSEs (Lapusta & Liu, 2009; Y. Liu & Rice, 2009) (D. Li & Liu, 2017; Perez-Silva et al., 2021).

For faults governed by rate-and-state friction, the quasi-static process zone at a non-zero rupture speed can be estimated as $\Lambda_0 = C \frac{\mu^* D_{RS}}{b \bar{\sigma}_n}$, where C is a constant of order 1 (Day et al., 2005; Jiang et al., 2022; Lapusta & Liu, 2009), $\mu^* = \mu$ for antiplane strain and $\mu^* = \mu/(1-\nu)$ for plane strain, where ν is Poisson's ratio. We note that our mesh size is considerably smaller than Λ_0 which ensures numerical stability and accuracy.

Table 1
Physical Parameters Used in the Quasi-Dynamic Slow-Slip Cycle Simulations

Parameter	Symbol	Value	Unit
Rate-and-state direct effect parameter ^a	a	0.01–0.02	–
Rate-and-state evolution effect parameter	b	0.0135	–
Characteristic slip distance (for SSEs)	D_{RS}^{SSE}	10.086	mm
Characteristic slip distance (for earthquakes) ^b	D_{RS}^{dy}	252.15	mm
Reference slip rate	v_0	10^{-6}	m/s
Reference friction coefficient	f_0	0.6	–
Initial slip rate	V_{ini}	10^{-9}	m/s
Initial state variable	θ_{ini}	0.1	s
Critical nucleation size	h_{RA}^*	112.3	km
Quasi-static process zone size	Δ_0	11.8	km
Effective normal stress	$\bar{\sigma}_n$	50	MPa
SSE effective normal stress	$\bar{\sigma}_n^{SSE}$	2.5	MPa
Lithostatic pressure	σ_z	depth-dependent	MPa
Pore fluid pressure	p_f	depth-dependent	MPa
Rock density	ρ	2670	g/m^3
Shear modulus	μ	30	GPa
Poisson's ratio	ν	0.25	–

^aParameter a varies between velocity-weakening to velocity-strengthening. ^bOur SSE cycle simulations do not include earthquakes.

We adopt the empirical “aging” law that can be interpreted to account for time-dependent healing of microscopic stationary frictional contacts (Beeler et al., 1996, e.g.), for describing the temporal evolution of state variable (θ):

$$\frac{d\theta}{dt} = 1 - \frac{V\theta}{D_{RS}}. \quad (4)$$

To regularize the solution at low slip rates we use the modification proposed by Rice and Ben-Zion (1996):

$$\mu = a \sinh^{-1} \left[\frac{V}{2v_0} \exp \left(\frac{\mu_0 + b \ln(v_0 \theta / D_{RS})}{a} \right) \right], \quad (5)$$

which is Equation 2 when $V \gg 0$.

A distribution of $(a - b)$ at different temperatures has been obtained from laboratory experiments for wet gabbro gouges (He et al., 2007). We project this temperature-dependent $(a - b)$ distribution onto the slab interface using the thermal profile from a 2D steady-state thermal model constrained by P-wave seismic tomography in central Mexico (Manea & Manea, 2011). We assume a downdip transition temperature, $(a - b) = 0$, of 415°C, which coincides with the maximum down-dip extent of long-term SSEs inferred from Global Positioning System (GPS) inversions (Radiguet et al., 2012). Velocity-strengthening conditions $(a - b) > 0$ are imposed at the two lateral sides of the model domain to stabilize slip toward the plate convergence rate. The distribution of $(a - b)$ across the entire slab is shown in Figure 2a. The physical parameters including friction, initial stress, and elastic material properties aforementioned are listed in Table 1.

2.2. 3D SSE-Initiated Dynamic Rupture Models for the Guerrero Earthquake

We use the open-source software *SeisSol* (<https://github.com/SeisSol>), which is based on the Arbitrary High-order Derivative (ADER) Discontinuous Galerkin (DG) finite element method, to perform simulations of earthquake rupture dynamics and seismic wave propagation (Dumbser & Käser, 2006; Käser & Dumbser, 2006; Pelties et al., 2012). *SeisSol* has been optimized for modern high-performance computing architectures including

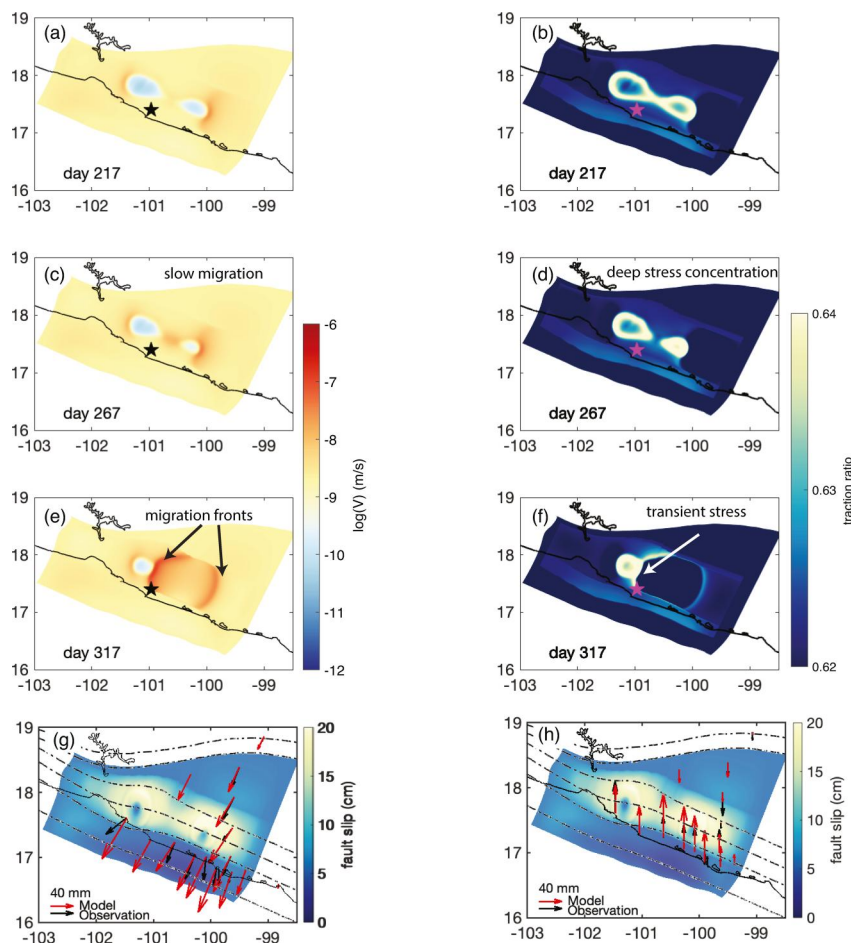


Figure 3. The 2014 Slow slip event (SSE) in the Guerrero Gap from the preferred quasi-dynamic slow-slip cycle model. Snapshots of fault slip rate (a, c, e) and traction ratios (b, d, f), defined as shear over effective normal stress, on days 217, 267, and 317, respectively. The black star marks the epicenter of the 2014 M_w 7.3 Guerrero earthquake from the National Earthquake Information Catalog (USGS NIEC) (<https://earthquake.usgs.gov/earthquakes/eventpage/usb000pq41/executive>). Slow-slip fault slip rates can reach up to 10^{-6} m/s, which is 1,000 times faster than the plate convergence rate ($V_{pl} = 61$ mm/yr). The time-dependent evolution of the fault slip rate is shown in Movie S1. (g, h): Modeled accumulated 2014 SSE fault slip distribution and surface Global Positioning System (GPS) displacement. The black and red arrows show the observed (Gualandi et al., 2017) and synthetic surface GPS displacements, respectively. Dashed black lines are the depth contours of the subducting slab from 20 to 80 km depth with 20 km depth spacing.

an efficient local time-stepping algorithm (Breuer et al., 2014; Heinecke et al., 2014; Krenz et al., 2021; Uphoff et al., 2017) and has been validated against several community benchmarks following the SCEC/USGS Dynamic Rupture Code Verification exercises (Harris et al., 2018; Pelties et al., 2014). Stress and particle velocities are approximated with 3rd-degree polynomials, yielding 4th-order accuracy in space and time during wave propagation simulation. We detail all dynamic rupture modeling parameters in the following.

2.2.1. Dynamic Rupture Initial Stresses

We constrain the initial stresses in the dynamic rupture model from a snapshot of the shear and effective normal stresses across the fault interface in the 2014 SSE model. We track the traction ratio as the slow-slip fronts migrate along-strike and find that the local peak in the hypocentral region appears on day 317 (Figures 3f and 4a). This local peak of traction ratio is associated with the acceleration of the migrating front from 0.5 km/day to 3 km/day (Figures 4b and 4c). The shear traction and effective normal stress on day 317 of the 2014 SSE quasi-dynamic model are saved and spatially interpolated onto the higher-resolution dynamic rupture mesh of the subduction fault surface using the package ASAGI (Rettenberger et al., 2016). The resulting ratio between the initial shear

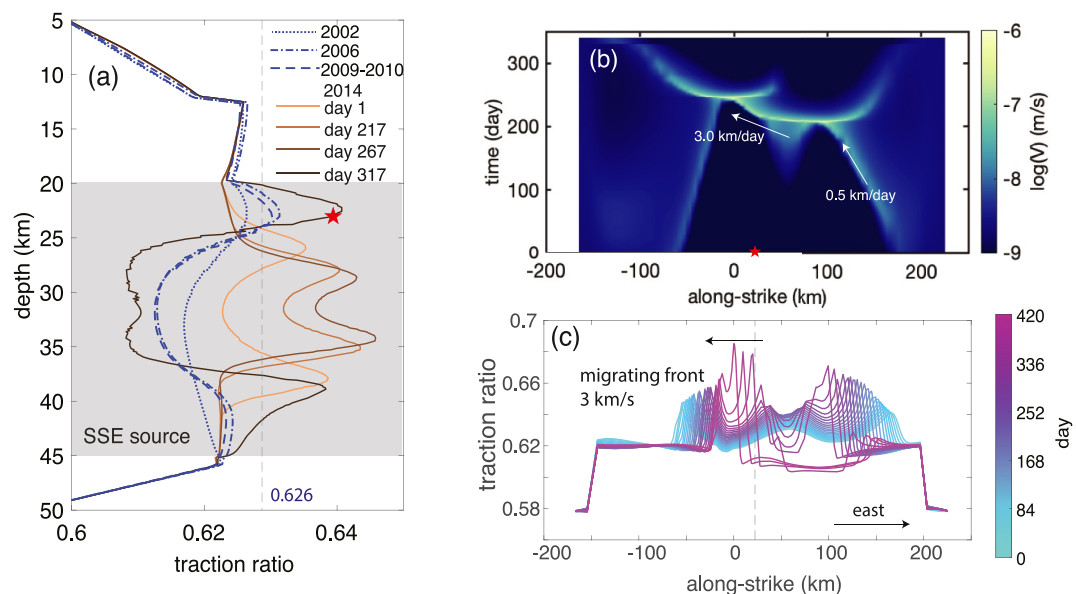


Figure 4. Time-dependent evolution of the on-fault shear-to-effective-normal traction ratio and along-strike migration speed during the modeled Slow slip event (SSE) cycle. The red star marks the USGS catalog hypocenter of the 2014 M_w 7.3 Guerrero earthquake. (a) Cross-sections of the traction ratio during the four modeled subsequent SSEs. Colored solid lines indicate the traction ratios on days 1, 217, 267, and 317 of the modeled 2014 SSE. The blue dot-dashed and dot-dotted lines represent the traction ratios of the three SSE episodes in 2002, 2006, and 2009–2010, respectively. The dashed gray line indicates the static friction coefficient on-fault ($\mu_s = 0.626$) assumed in the dynamic rupture earthquake simulation. (b) Spatial and temporal evolution of the on-fault slow-slip rate along the 20 km depth contour. The white vectors indicate the averaged migrating speeds of the slip front at $y = 150$ km and $y = 0$ km. (c) Profiles of the traction ratio sampled every 10 days along the 30 km depth contour during the modeled SSE cycle illustrate the westward acceleration of the SSE migration front.

and effective normal stress is shown in Figure 3f. The time-dependent evolution of the traction ratio parameter on the fault during the modeled SSE is shown in Movie S2.

2.2.2. Velocity Structure

We use a 1D depth-dependent model of the density and seismic velocities to set the elastic properties (μ and λ) in the dynamic rupture model, as shown in Figure S9 in Supporting Information S1 and Figure 1b. This 1D velocity model is based on seismic imaging of the central Mexico subduction zone (Dougherty & Clayton, 2014) using the Mapping the Rivera Subduction Zone (MARS) seismic array, which consists of 50 broadband seismic instruments with a station spacing of \sim 40 km deployed from January 2006 to June 2007. This 1D layered velocity structure captures the major features of the subsurface (Kim et al., 2010; Song et al., 2009).

2.2.3. Asperities

In the 3D dynamic rupture simulations, we adopt a linear slip-weakening (LSW) friction law to constrain the fault frictional strength which has been shown to largely depend on the fault slip distance in laboratory experiments (Ida, 1972; Palmer & Rice, 1973) (Table 2). LSW friction laws have been widely used in dynamic rupture simulations including models of large megathrust earthquakes such as the 2004 M_w 9.1–9.3 Sumatra–Andaman earthquake (Ulrich et al., 2022; Uphoff et al., 2017), 2011 M_w 9.0 Tohoku-Oki earthquake (Galvez et al., 2014), and rupture scenarios for the Cascadia subduction zone (Ramos et al., 2021). While SeisSol offers using various rate-and-state-friction laws, we opt for LSW friction due to its computational efficiency and fewer parameters. Although using rate-and-state friction as in the SSE cycle simulation may seem more consistent, differences in time stepping and time integration methods across numerical techniques can introduce inconsistencies as well (Liu et al., 2020).

Fault friction initial conditions are difficult to constrain on the scale of megathrust slip but play an important role in dynamic rupture nucleation and propagation (Ulrich et al., 2022; van Zelst et al., 2019). Based on several trial

Table 2
Linear Slip-Weakening Friction Parameters Used in the Dynamic Earthquake Rupture Simulations

Parameter	Symbol	Distribution	Value
Static friction coefficient	μ_s	Uniform	0.626
Dynamic friction coefficient	μ_d	Two asperities	0.546
Critical slip distance	d_c	Uniform	0.05 m
Frictional cohesion	c_0	Depth-dependent	1.0–0 MPa

dynamic rupture scenarios we set the static friction coefficient to $\mu_s = 0.626$ and the dynamic friction coefficient to $\mu_d = 0.546$ within the assigned rupture asperities which yield realistic co-seismic rupture dynamics and arrest as well as spontaneous nucleation at a depth of 22 km due to the 2014 SSE stressing. Our choice of static friction allows for a smooth nucleation process at the hypocenter without introducing additional overstress and is within the range of effective static friction typically used in dynamic rupture megathrust scenarios (Galvez et al., 2014; Madden et al., 2022; Ramos & Huang, 2019). We assume depth-dependent frictional cohesion c_0 and constant critical slip distance d_c (Text S1 in Supporting Information S1).

We assume a statically strong fault (static friction coefficient $\mu_s = 0.626$) in agreement with the high static frictional strength of rocks (Byerlee, 1978) but effectively weakened by high pore fluid pressure. This specific choice of μ_s allows us to model realistic co-seismic rupture dynamics and arrest, including realistic levels of slip, rupture speed, and stress drop, as well as spontaneous nucleation at 22 km due to the modeled 2014 SSE event. The selection of dynamic friction is constrained by matching both the seismic source time function and the geodetic static surface displacements while ensuring a smooth rupture arrest. Figure S8 in Supporting Information S1 shows that the steady state rate-state friction at coseismic slip rates in the seismogenic zone is corresponding to the dynamic friction value in the LSW law. In our preferred model (referred to as Model A1), we include two asperities, constrained by the two peaks in moment rate function revealed in kinematic source inversion (Ye et al., 2016). We use a constant μ_d within each asperity. An increase in μ_d outside the asperities is required for smooth and spontaneous rupture arrest (Text S2 in Supporting Information S1). We find that by increasing μ_d to values 30% ($\mu_d = 0.826$) higher than μ_s , dynamic rupture gradually stops at the edges of the asperities. This setup results in a comparable duration and peak of moment release to teleseismic inversion (Ye et al., 2016) (Figure 6a). The on-fault distribution of μ_d following $0.826 - 0.28 \times G_1(r_1, r_2)$ is shown in Figure 6f.

3. Results

3.1. The 2014 M_w 7.6 Slow-Slip Event on the Curved and Fluid-Rich Flat Slab of the Guerrero Gap

We model cycles of long-term SSEs (Text S2 in Supporting Information S1) and select four sequential events that occur repeatedly every 4 years. During the 200-year simulation, the recurring times range between 1 and 5 years (Figure S9 in Supporting Information S1). Figure 3 shows snapshots of the fault slip rate in the modeled scenario of the 2014 SSE. Each SSE episode lasts for up to 12 months (Radiguet et al., 2012) and reaches a peak slip rate of up to 10^{-6} m/s (Figures 3a–3c and 3e). Our numerical results match the region-specific source characteristics of long-term SSEs inferred from geodetic inversion using the regional GPS network (Radiguet et al., 2016) (Table S1 in Supporting Information S1). We attribute the good match of the first-order SSE characteristics to the realistic flat slab geometry and assumed near-lithostatic pore fluid pressure (D. Li & Liu, 2016; Perez-Silva et al., 2021). We select four sequential SSE episodes of our model, closely corresponding to the four geodetically recorded events in 2001/2002, 2006, 2009/2010, and 2014. We calculate the horizontal and vertical components of synthetic surface displacements at regional GPS stations and compare them with geodetic inversions (Gualandi et al., 2017; Radiguet et al., 2012). The comparison between the synthetic and observed GPS vectors during the 2014 SSE is shown in Figures 3g and 3h and for the three earlier SSE episodes in Figure S7 in Supporting Information S1. All modeled SSE events yield good agreement with geodetic observations, although only dip-slip is considered in our simulations (D. Li & Liu, 2016).

The 2014 SSE initiates simultaneously at the eastern and western edges of the Guerrero Gap at a depth of 40 km. Both slip fronts migrate toward the center at a rate of 0.5 km/day (Figures 3a and 4b). The megathrust slips at a higher rate after the coalescence of the migrating fronts in the center, and the SSE then bilaterally propagates across the entire fault between 25 and 40 km depth. However, we observe no immediate coseismic slip nucleating upon coalescence of the SSE fronts (between a depth of 20–45 km). This is different from the results of earlier 2D planar fault simulations (Kaneko et al., 2017) but in agreement with recent on- and off-shore observations that find no evidence of coseismic rupture due to collapsed slow-slip migrating fronts in the Guerrero Gap (Plata-Martinez et al., 2021).

Figure 4 shows the time-dependent evolution of the on-fault shear-to-effective-normal traction ratio and along-strike migration speed during the cycle of all four SSEs. During the quasi-periodic emergence of the SSEs, we

find that fault shear tractions overall increase down-dip of the seismogenic zone (below a depth of 20 km). However, this increase is not steady and varies considerably with the acceleration of the migrating slip fronts. The space-time evolution of the traction ratio, defined as the shear over effective normal stress during the modeled transient slip, is shown in Figures 3b–3d and 3f. Here, the traction ratio increases gradually from down-dip (30 km depth) to up-dip (20 km depth) and eventually reaches 0.64 in the hypocentral area of the 2014 M_w 7.3 earthquake at a depth of 22 km, which is slightly shallower than that inferred by the USGS (Figures 3f and 4a).

The migrating 2014 SSE front moves slowly until day 267 and accelerates to 3.0 km/day at day 317 (Figure 4b). This acceleration, associated with rapid strain energy release, eventually increases shear stress at the down-dip end of the seismogenic zone in our model (see Figure 4c and Movie S2). The migration speed can vary depending on the temporal evolution of stress and stressing rate during the modeled SSE, which results in various values of traction ratio below the locked zone between different slow-slip cycles (Figure S5 in Supporting Information S1). Accelerating SSE fronts, as in our 2014 SSE model, have been observed before the 2014 Chile earthquake (Socquet et al., 2017a) and before larger earthquakes in Japan (Uchida et al., 2016), which was suggested as a potential precursory signal initiating megathrust earthquake nucleation.

In contrast, traction ratios increase considerably less during the earlier three modeled SSEs (blue lines in Figure 4a and blue-to-purple lines in Figure S4 in Supporting Information S1). Shear stresses temporally increase during the 2001/2002 and 2006 SSEs but decrease during the 2009/2010 event. For example, the peak traction ratio in the 2014 episode is about 3.23% higher than in the preceding 2009–2010 event, corresponding to a 0.1 MPa increase in shear stress. We highlight that the long-term increase of the peak traction ratio at the hypocentral depth during the 20-year-long simulation is small compared to the transient traction changes during the 2014 SSE (Figure 4a). None of the three earlier events leads to traction ratios large enough to overcome the (prescribed) frictional fault strength in the seismogenic part of the slab in our preferred dynamic rupture model.

In our 200-year long-term SSE cycle simulation there appear no earlier SSEs with comparable magnitude and recurrence intervals to our selected sequence and earlier transient stresses are insufficient to initiate a megathrust rupture in our model configuration (Figure S18 in Supporting Information S1). The long-term stress loading is accommodated by very long-term, low-amplitude slow slip episodes within the seismogenic zone. This modulates the stressing at seismogenic depth with a recurrence time of 100 years but causes no coseismic rupture (Figure S1 in Supporting Information S1). These long-lasting events accommodate a considerable fraction of the total accumulated strain within the shallow seismogenic zone, consequently limiting the shallow peak slip rates in the dynamic rupture simulation. The lack of shallow coseismic slip in our slow slip cycle simulation aligns with recent evidence for shallow fault creep off-shore Guerrero (Plata-Martinez et al., 2021). However, due to uniform plate loading rate and a lack of earlier geodetic constraints, we cannot rule out alternative models in which potential earlier SSEs may meet the megathrust's frictional yielding criteria.

We present the first 3D dynamic rupture model of the 2014 M_w 7.3 Guerrero earthquake. Our rupture scenarios are informed by the transient stress of preceding SSEs when the peak of the traction ratio reaches the hypocenter (Figure 4) and additional predefined frictional heterogeneity on the fault. We focus on a preferred model (Section 2.2; Figure 5) which uses an LSW friction law (Andrews, 1985) to describe the co-seismic fault strength and yielding. The specific choice of a critical slip-weakening distance of $d_c = 0.05$ m and a statically strong fault (static friction coefficient $\mu_s = 0.626$) ensures that the model that reproduces the key features of geophysical observations and provides physically self-consistent descriptions of earthquake initiation, dominantly governed by SSE-induced shear stress changes, and its dynamics and arrest, which are predominantly governed by predefined frictional asperities. We discuss alternative rupture scenarios, including one less realistic model with smaller μ_s as shown in Figure S15 in Supporting Information S1, probing sensitivity to initial conditions in Section 4.2.

Although earthquake nucleation is linked to the transient stress of the SSE cycle, we show that capturing realistic rupture propagation and arrest requires additional heterogeneity of the megathrust slab. We show that including two circular frictional asperities (Section 2.2.3) can reproduce the observed co-seismic characteristics to first-order. We vary the maximum possible frictional strength drop smoothly within each asperity: the dynamic friction coefficient μ_d gradually increases at the edge of the asperities. High variability of dynamic friction has been reported in relation to fault materials and sliding rates in laboratory experiments (Collettini et al., 2019; Di Toro et al., 2004) and has been shown to largely affect coseismic rupture dynamics on crustal faults in numerical models (Aochi & Twardzik, 2020; Ramos & Huang, 2019).

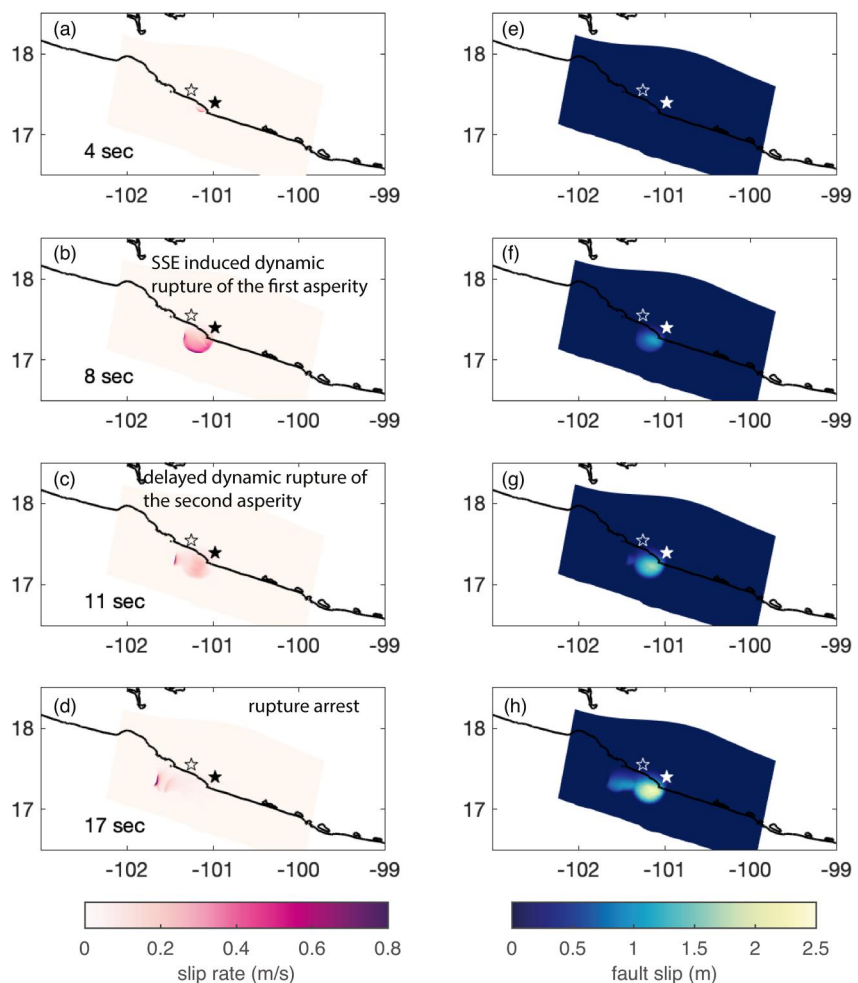


Figure 5. Preferred dynamic rupture model of the 2014 M_w 7.3 Guerrero earthquake. Snapshots of the modeled coseismic fault slip rate (left panels) and fault slip (right panels) at 4 s, 8 s, 11 s, and 17 s, respectively. (a): spontaneous nucleation governed by shear stress transients of the long-term Slow slip event (SSE) cycle, (b): SSE-initiated dynamic rupture of the first asperity, (c): delayed rupture of the second asperity, and (d): the dynamic arrest of rupture (Movie S3). The corresponding fault slip at each time step is shown in panels (e–h), respectively. The coastline is indicated by the black line. Solid and empty stars indicate the different hypocenter locations from the USGS and GCMT catalogs, respectively.

In our earthquake model, self-sustained dynamic rupture nucleates spontaneously at a depth of 22 km, where the modeled 2014 SSE front acceleration leads to a local increase in shear traction (Figures 4a–4c). This location agrees with the observationally inferred hypocenters within their uncertainties (Figures 5a and 5b). Unlike typical dynamic rupture models, where nucleation is prescribed ad hoc (e.g., Galis et al., 2014), spontaneous runaway rupture is initiated merely by the locally increased shear stress of the preceding SSE transient. Our rupture model dynamically breaks the central asperity and subsequently migrates to the second patch under slightly increasing slip rates (Figure 5 and Movie S3). The rupture arrests smoothly at the boundaries of the prescribed frictional asperities. The final rupture area is located up-dip from the hypocenter and has no clear overlap with the area that hosts aseismic rupture during slow slip (Figure S10 in Supporting Information S1).

Our preferred earthquake simulation resembles the key observed seismic and geodetic characteristics within observational uncertainties (Figures 6a–6e). Two broad peaks in the moment release rate emerge in our dynamic rupture model, as inferred from teleseismic inversion using more than 70 stations across 35° – 80° epicentral distance (Ye et al., 2016) (Figure 6a). This suggests a multi-asperity rupture process, including dynamic triggering and delays between different asperities (Figure 6f). In our rupture dynamics model, the first and second peaks appear closer in time than inferred in the inversions which may reflect additional complexities on natural faults and observational uncertainties. For example, the shape of the second asperity area may be varied in our

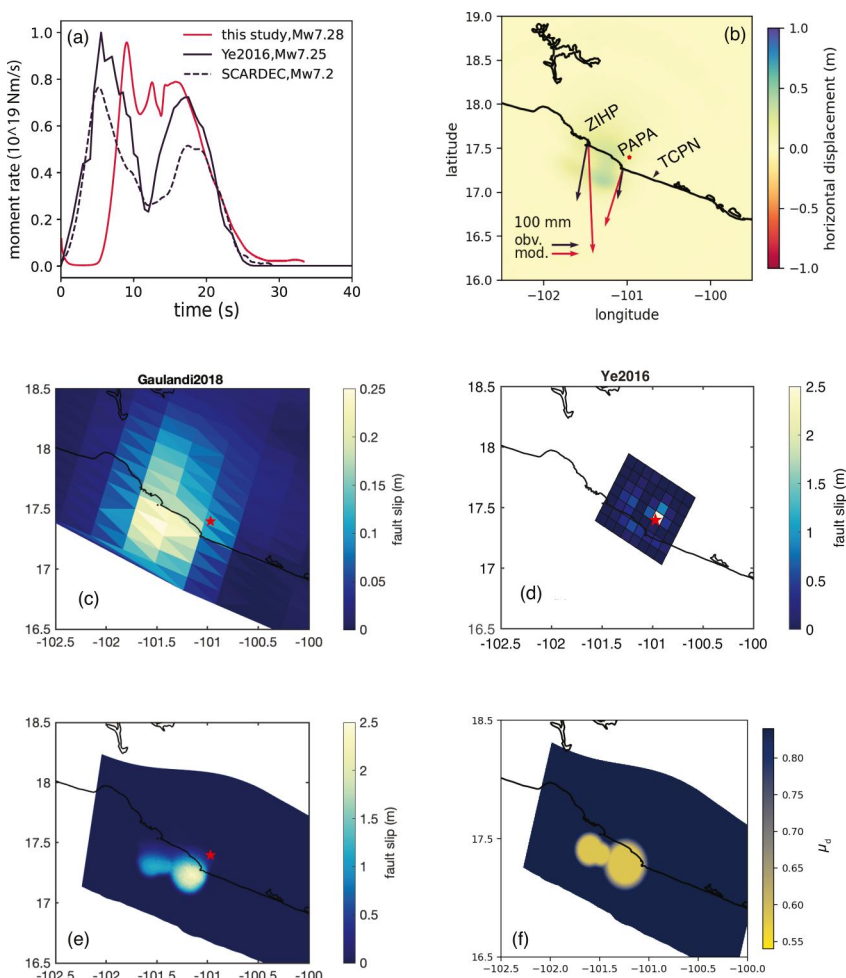


Figure 6. Observational verification of kinematic and dynamic source characteristics of the dynamic rupture model of the 2014 M_w 7.3 Guerrero earthquake. (a) On-fault dynamic rupture moment rate compared to teleseismic inversion (Ye et al., 2016) and SCARDEC (<http://scardec.projects.sismo.ipgp.fr>) (Vallee et al., 2011). (b) Mapview with horizontal surface displacements observed at continuous Global Positioning System stations (black) Gualandi et al. (2017) and in our simulation (red). The red star marks the USGS catalog hypocenter. Accumulated fault slip from (c) regional geodetic inversion (Gualandi et al., 2017), (d) teleseismic inversion (Ye et al., 2016), and (e) preferred dynamic rupture scenario. The maximum slip is 0.25 m, 2.5 and 2.5 m, respectively. (f) Distribution of the prescribed heterogeneous dynamic friction coefficient μ_d which gradually increases from 0.546 within to 0.826 at the edge of the asperities following an exponential function (see Methods: “Linear slip-weakening friction”).

dynamic rupture model to better match the observed moment rate release timing. However, teleseismic inversion lacks the adequate resolution to better inform on the spatial extent of slip (Ye et al., 2016). Our modeled total cumulative moment release is 9.41×10^{19} Nm, which corresponds to a moment magnitude of M_w 7.28 and agrees well with the observations (Figure 6a). An alternative dynamic rupture model with only a single asperity (Section 4.2; Figure 7) fails to reproduce a realistic moment magnitude and the pronounced two-peak character of the moment rate release. Because both dynamic rupture models spontaneously initiate due to the same transient SSE stresses but strongly differ in co-seismic dynamics, we conclude that additional frictional heterogeneity is required to model the propagation dynamics and arrest of the Guerrero earthquake.

Geodetic inversion using permanent on-shore GPS stations yields smaller slip amplitudes (Gualandi et al., 2017) but a larger rupture area extending up to the trench, compared to teleseismic inversion (Ye et al., 2016) (Figures 6c and 6d). Similarly, our modeled dynamic rupture features shallow fault slip up-dip of the hypocenter, while our maximum slip amplitude is 2.5 m (Figure 6e), which is consistent with teleseismic inversion assuming $V_r = 2.5$ km/s (Ye et al., 2016). We note that the differences in geodetic and teleseismic fault slip inversions are likely affected by limitations in data resolution and differences in the assumed source time functions, velocity

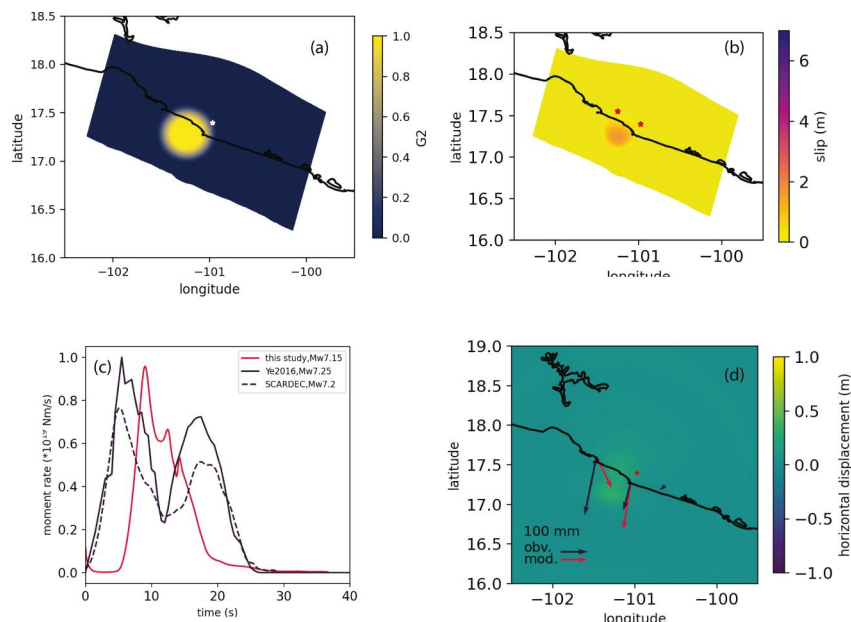


Figure 7. (a) Map view of the exponential function G_2 which we use to prescribe the single asperity of Model B1. (b) Cumulative fault slip, (c) moment release rate, and (d) synthetic surface deformation of dynamic rupture Model B1 with a single asperity. The shown Global Positioning System stations are the same as in Figure 6b.

models, and/or fault geometries. Figure 6b shows the modeled static surface deformation at 80 s after the rupture initiation and its comparison with geodetic observations (Gualandi et al., 2017). There are only two GPS stations (ZIHP and PAPA) with clear recorded signals close to the rupture area and one station (TCPN) with a smaller-amplitude signal distant from the epicenter. Our synthetic surface displacements at ZIHP and PAPA are consistent with the reverse plate movement direction but slightly higher in amplitude than those observed.

Our preferred two-asperity dynamic rupture model reproduces both seismic and geodetic characteristics and is consistent with the localized slip heterogeneity inferred from seismic imaging using regional networks (Plata-Martinez et al., 2021; Song et al., 2009). Given the sparsity of co-seismic seismic and geodetic observations, we judge our forward model as data-justified first-order illumination of rupture dynamics and arrest. We note that future incorporation of a high-resolution regional velocity model, affecting the non-linear, coupled dynamics of rupture dynamics process and seismic wave propagation, may improve the achieved observational match.

We analyze the stress drop and energy budget of our preferred dynamic rupture model accounting for the preceding slow-slip cycle with respect to event-specific and global observations (Text S2 in Supporting Information S1). We calculate the average co-seismic stress drop in two different ways: (a) by spatially averaging the on-fault stress drop, and (b) by averaging the modeled stress drop based on energy considerations (Noda et al., 2013; Perry et al., 2020). The two approaches result in average model stress drops of 1.74 and 2.1 MPa, respectively. These values are within the expected uncertainties (Abercrombie, 2021) of the seismological inference of 2.94 MPa (Ye et al., 2016) and are consistent with the global average of the inferred megathrust earthquake stress drops (Abercrombie & Rice, 2005).

Next, we analyze the earthquake initiation energy budgets accounting for the transient stress shadowed by the preceding SSE. We calculate the average fracture energy across the effective nucleation area directly induced by our modeled 2014 SSE in the hypocentral area as 0.17 MJ/m^2 (Text S2 in Supporting Information S1).

This inference is comparable to the range of nucleation energies ($0.1\text{--}1 \text{ MJ/m}^2$) estimated for most $M > 8$ Nankai earthquakes in southwestern Japan (N. Kato, 2012), implying that the transient stresses of aseismic slip may play a ubiquitous role in the nucleation of megathrust earthquakes. In comparison, the dynamic rupture fracture energy averaged across the entire co-seismically slipping fault is only 0.11 MJ/m^2 . This is about 35% lower than the SSE fracture energy at the hypocenter governing the nucleation stage and similar to a seismologically inferred global average of $0.1\text{--}10 \text{ MJ/m}^2$ (Abercrombie & Rice, 2005), but 45% lower than the range of $0.2\text{--}2.0 \text{ MJ/m}^2$ measured

on natural crustal faults (Tinti et al., 2005). This relatively low overall fracture energy is consistent with the low average stress drop, which results from the assumed elevated pore fluid pressure constrained by regional seismic imaging (Song et al., 2009). The elevated pore fluid pressure at depth is crucial for recovering faulting dynamics during both the long-term SSE and short-term initiation of our dynamic rupture model.

In addition to shear stress amplitudes, also the shear stressing rate increases significantly with increasing slip rate during the 4th SSE, and we observe a pronounced peak five days before the linking date (day 317, Figure S6 in Supporting Information S1). Shear stressing rates also change at the onset of the first and second SSE, but remain smaller or negative, and the peak amplitude of shear stress is lower during the 3rd event. Although temporal changes in shear stressing rate are not included in the dynamic rupture nucleation process, our linked model may suggest that the increasing stressing rate associated with the migrating fronts might be a proxy for an accelerating aseismic signal (Uenishi & Rice, 2003). have shown that the spontaneous nucleation governed by LSW friction is independent of the distribution of loading stresses or stressing rates as long as stress reaches the peak fault strength over a sufficiently wide region. However, the critical nucleation size of real events may depend on loading rate according to laboratory and numerical experiments using rate-and-state friction laws (Guérin-Marthe et al., 2019; Kaneko et al., 2008).

4. Discussion

4.1. Transient Influence of Slow Slip on the Initiation of Megathrust Earthquakes

Our dynamic rupture models of the $M_w 7.3$ Guerrero earthquake initiated by quasi-dynamic models of the preceding long-term SSE cycles illustrate the interaction between aseismic and co-seismic fault slip. It has been suggested that slow slip at the down-dip end of the seismogenic zone transfers shear stresses up-dip (Y. Liu & Rice, 2007) or temporally aid up-dip pore fluid migration (W. Frank et al., 2015), both of which potentially destabilize the locked portion of the megathrust, eventually triggering co-seismic rupture (e.g., Cattania & Segall, 2021) and increasing regional seismicity (e.g. Y. Liu & Rice, 2009). The kinematic migration patterns of off-shore aseismic slip are often challenging to constrain due to the lack of dense geodetic observations. Sequences of foreshocks and migrating seismicity before large events such as the 2011 Tohoku-Oki earthquake have been interpreted as proxies for aseismic fault slip and as potential long-term precursory signals of megathrust earthquake nucleation processes (A. Kato et al., 2012). Other observations of possible precursory signals include the acceleration of a $M_w 6.5$ SSE that was recorded by the land-based GPS stations 8 months before the 2014 $M_w 8.1$ North Chile earthquake (Socquet et al., 2017a).

We find that the transient increase in the shear-to-effective-normal-stress ratio resulting from the accelerating migration of the preceding slow-slip events can lead to the spontaneous initiation of realistic earthquake rupture and that this process is sensitive to the dynamics of the long-term transient SSE cycle. In our model, the increasing transient shear stress is sufficiently high for spontaneous dynamic rupture without additional weakening mechanisms, such as the effects of thermal pressurization (Noda et al., 2009). The total SSE-induced shear stress increase is ≈ 0.021 MPa, the difference between shear stress and yielding strength, in the hypocentral area. Figure S17 in Supporting Information S1 shows an alternative 3D dynamic rupture scenario in which, instead of using the transient stresses induced by slow slip, we prescribe an ad hoc time-dependent rupture initiation (following, e.g., Harris et al., 2018) as a weaker, spherical patch, centered at the hypocenter. The SSE transient stresses are not only large enough to nucleate earthquake dynamic rupture but also affect 3D rupture dynamics. Figures S17c and S17d in Supporting Information S1 show the resulting in shorter rupture duration, lower moment magnitude, and less complex moment rate release function due to reduced rupture complexity.

However, accounting for additional co-seismic weakening may further aid the slow-slip transient initiation of dynamic rupture (Hirono et al., 2016) inherently capturing our here prescribed variability of co-seismic frictional strength drop (Perry et al., 2020). Similarly, a recent conceptual model combining shallow SSEs and two asperities finds that the time-dependent balance between stress and strength is complex and not all SSEs directly lead to the nucleation of an earthquake (Meng & Duan, 2022), even when no geometrical complexity or pore fluid variation is considered.

For simplicity, we assume constant pore-fluid pressure during our geodetically constrained slow slip cycle modeling. Future work may explore the additional effects of dilatancy that may stabilize co-seismic slip (Segall et al., 2010) and may affect the overall slip budget at the downdip limit of the seismogenic zone (Y. Liu &

Rubin, 2010; Y. J. Liu, 2013). The effects of dilatancy and permeability enhancement in highly permeable fault zones may alter aseismic slip (Yang & Dunham, 2023). Dal Zillo et al., 2020 consider dilatancy to model SSEs in a planar Cascadia model and find slightly slower down-dip rupture speed and longer event durations, which may affect megathrust earthquake nucleation.

4.2. Alternative Dynamic Models With Varying Asperities

Accounting for megathrust asperities in our co-seismic dynamic rupture model is important for reproducing observationally inferred first-order source characteristics. Our preferred dynamic rupture scenario includes two frictional asperities (Figure 6f), which vary in their local dynamic friction coefficient from the surrounding slab interface, as proxies of megathrust heterogeneity governing the co-seismic rupture complexity. Simpler numerical model setups lend themselves to parameter space exploration (Y. Liu & Rubin, 2010; Ampuero & Rubin, 2008). While we here do not aim to cover the range of all possible initial condition variations in our complex model setup, we show two selected alternative dynamic rupture scenarios that illustrate the sensitivity of our SSE-initiated co-seismic rupture dynamics to prescribed frictional asperities. Our SSE cycle model is the preferred model out of five different long-term SSE cycle simulations (SI, Perez et al., 2019).

4.2.1. Model A2: Two Rupture Asperities With Higher Initial Shear Stress

In dynamic rupture simulations, asperities due to locally reduced dynamic frictional strength lead to similar rupture behavior as asperities of elevated initial shear stress due to the equivalent fracture energy. Here, we present an alternative dynamic rupture model, Model A2, with a constant dynamic friction coefficient but heterogeneous initial shear stress. The initial shear stress is smoothly reduced outside both rupture asperities, which leads to spontaneous rupture arrest. We use the same spatial exponential function $G_1(r_1, r_2)$ defined in Text S2 in Supporting Information S1 to decrease shear stresses smoothly outside the two geometrically equivalent pre-assigned rupture asperities. We set the initial shear stress as $\tau_0^{A2} = \tau_{sse} \times G_1(r_1, r_2)$ where τ_{sse} refers to the on-fault shear stress linked from the SSE cycle model (Figure S12a in Supporting Information S1). This setup leads to a localized distribution of the shear-to-effective-normal-stress ratio near the USGS catalog hypocenter (Figure S12b in Supporting Information S1).

The modeled source characteristics of the earthquake, including moment release, magnitude, slip distribution, and surface deformation, are all similar to our preferred model (Figure S14 in Supporting Information S1), except for a slightly sharper peak in moment release, corresponding to rupture arrest, than that of our preferred model (Model A1). We conclude that, in principle, local shear-stress asperities can lead to equivalent SSE-initiated rupture dynamics compared to frictionally-weak asperities.

4.2.2. Model B1: A Single Rupture Asperity With Reduced Dynamic Friction Coefficient μ_d

Next, we demonstrate the sensitivity of rupture dynamics and synthetic observables (e.g., moment rate release) to megathrust heterogeneity using a single circular asperity wherein the dynamic frictional strength locally decreases (Model B1).

We examine a model with a single asperity with varying μ_d on the fault. We manually introduce an exponential taper function, called $G_2(r_1)$, similar to G_1 defined in Text S2 in Supporting Information S1 on the fault. The distribution of dynamic friction shaped according to function G_2 is shown in Figure 7a.

$$G_2(r_1) = \begin{cases} 4/3.0 * \min\left(0.75, \exp\left(\frac{r^2}{r^2 - r_{c1}^2}\right)\right) & r_1 \leq r_{c1} \\ 0 & \text{otherwise} \end{cases}$$

where r_{c1} are 38 km, $r_i = \sqrt{(x - x_i)^2 + (y - y_i)^2}$, $i = 1$. The positions of centers are listed in Table S2 in Supporting Information S1. The results of Model B2 are shown in Figures 7b–7d.

The resulting moment magnitude is only $M_w 7.15$, and the moment rate release features a single sharp peak instead of reproducing the observed characteristic two-peak shape (Figure 7c). The modeled spatial extents of the fault slip and surface displacement amplitudes are significantly smaller (Figures 7b–7d).

4.3. Variation in Fault Asperities and Its Implication for Seismic Hazard

Megathrust asperities have been related to depth-varying seismic and aseismic faulting behaviors (Lay et al., 2012; Walton et al., 2021). While we here parameterize both asperities as dynamically weak (low μ_d), heterogeneity in the initial stresses, structure, effective static fault strength, or pore fluid pressure (Bilek & Lay, 1999; Bürgmann, 2018) may serve as dynamically viable asperities (Harris et al., 2021; Madden et al., 2022; Ramos & Huang, 2019) and additional observations are required to distinguish between them. We show that local shear-stress asperities can lead to equivalent rupture dynamics in Section 4.2 and Figure S14 in Supporting Information S1. Our parameterization of frictional asperities is relatively simple but effective in reproducing first-order characteristics within the uncertainties of sparsely observed earthquake kinematics. With improved observational coverage, better-constrained seismic and geodetic fault slip inversion may provide better information on frictional asperities. Such smaller-scale stress or frictional strength heterogeneity may lead to a more complex rupture process: Laboratory experiments, geodetic measurements, and seismological observations imply that additional small-scale heterogeneity and physical processes, such as variations in rheology (Gao & Wang, 2017), frictional properties (Lay et al., 2012), as well as pore fluid effects (Zhu et al., 2020) may impact the coseismic behavior. Denser regional seismic and geodetic instrumentation along the central Mexican coast and off-shore, allowing for better imaging of coseismic fault slip, would be crucial to inform and validate data-integrated and physics-based modeling.

Our choice of frictional parameters in the dynamic rupture model allows for balancing the depth-dependent fault strength, heterogeneous initial shear stresses, and heterogeneous frictional strength drop to achieve realistic levels of coseismic slip and moment release across a relatively small rupture area in dynamic rupture simulations. Varying the, in LSW friction well-defined, static friction coefficient impacts our match of the observed smooth acceleration in the moment rate function. Given the heterogeneous shear stress perturbation of the preceding SSEs, a well-defined yielding strength is helpful to understand spontaneous dynamic rupture nucleation to first order. This sensitivity is exemplified in Figure S15a in Supporting Information S1 where a slightly lower μ_s results in delayed rupture arrest, a larger rupture area, and over-prediction of the amplitude and arrival of the first peak in the modeled moment release. Although simpler than the rate-and-state friction law used in the long-term SSE cycle simulations, we yield a similar range in reference friction coefficients (Figure S15b in Supporting Information S1) and comparable behavior in coseismic slip.

Our models help interpret geodetic and seismological observations of slow slip and coseismic megathrust rupture and help to unravel their interaction using available observations in Guerrero. We identify the acceleration of slow slip migration fronts as a driving mechanism preceding the initiation of coseismic rupture in our models. This may have important implications for enhancing the understanding of precursory slow slip, seismicity, and megathrust earthquakes in other subduction zones, such as in Japan (A. Kato et al., 2012). While our models do not enable the prediction of the relationship between long-term slow slip and future earthquakes, we anticipate our findings will also enhance the understanding of observed signals associated with the spectrum of megathrust faulting.

Our modeled SSE and coseismic fault slip are located largely off-shore in central Mexico, where a dense array of ocean bottom seismometers has discovered episodic shallow tremors, suggesting small-scale slow-slip events or low-frequency earthquakes (Plata-Martinez et al., 2021) potentially linked to small asperities up-dip of the slow-slip region. Accounting for additional small-scale heterogeneity on the fault may help explain high-resolution observations, such as complexity in moment release rate and strong ground motions (Galvez et al., 2016). Here, we focus on the one-way interaction between the SSE cycle and dynamic rupture and omit the respective influence of coseismic rupture on slow-slip transients. Modeling 3D fully dynamic earthquake cycles on geometrically complex faults (Erickson et al., 2023; Jiang et al., 2022) that incorporate spontaneous (aseismic) nucleation, dynamic rupture, and post-seismic deformation are computationally challenging but are becoming achievable at realistic scales and levels of complexity to allow for direct observational verification. Extending our approach to a unified and fully coupled slow-slip and dynamic rupture framework is a promising future step.

4.4. Model Limitations

We discuss the choice of linear-slip weakening friction in our dynamic rupture simulation by comparing key controlling factors of earthquake nucleation, the equivalent static friction coefficient (μ_s^{RS}) and slip-weakening rate (W , as defined by Uenishi and Rice (2003)) between our 3D slow slip cycle and dynamic rupture models.

Coseismically, the slip-dependent fault weakening behavior governed by aging law rate-and-state friction is similar to that governed by LSW friction as has been shown in theoretical and numerical analysis (e.g., Bizzarri & Cocco, 2003; Garagash, 2021; Kaneko et al., 2008). We estimate an equivalent peak rate-and-state static friction coefficient μ_s^{RS} using the relation $\mu_s^{RS} \approx f_p = f_0 + a \ln(V_{sr}/V_0)$ (Garagash, 2021) and assuming slip rates ranging between $10^{-9} - 10^{-7}$ m/s during the slow slip cycle simulation and $a = 0.01$. The such estimated peak value is $\mu_s^{RS} = 0.62$, comparing well with $\mu_s = 0.626$ used in our linear-slip weakening dynamic rupture model.

Following Garagash (2021), we can estimate the equivalent linear-slip weakening D_c from aging law rate-and-state frictional weakening near the rupture front as $D_c \approx 5.8$ m, with constant $b = 0.0135$, $\bar{\sigma} = 50$ MPa. We can also compare the equivalent critical slip distances assuming slip-law rate-and-state friction, following Uenishi and Rice (2003) by equaling the slip weakening rates for our frictional parametrizations of both models, defined as $\Delta\tau/D_c = W^{LSW}$ and as $b\bar{\sigma}/D_{RS} = W^{RS}$ with $\Delta\tau = (\mu_s - \mu_d)\bar{\sigma}$, which results in $D_c/D_{RS} = 5.93$, implying an equivalent $D_c \approx 1.5$ m in linear slip weakening friction.

However, we find that our linked dynamic rupture model requires a small $D_c = 0.05$ m (cf. Figure S16 in Supporting Information S1), resulting in a slip weakening rate of 77.9 MPa/m. This discrepancy may express different megathrust frictional behavior governing regions hosting SSE and dynamic rupture and could be further explored in future work, including additional physics or heterogeneity, for example, scale-dependent fracture energy (Gabriel et al., 2023; Ide & Aochi, 2005), alternative long-term friction evolution models (T. Li & Rubin, 2017), or analytically accounting for the rupture speed dependence of the aging law equivalent linear-slip weakening estimates. We note that matching dynamic friction may be less crucial since additional weakening mechanisms can be active at coseismic slip rates (e.g., Di Toro et al., 2011) and we caution that we here do not fully explore the effects of self-consistent parameterization on the interaction between slow slip and dynamic rupture simulations.

We simplify the complex physics and initial conditions in our models of SSEs and dynamic rupture in several ways. The long-term slow slip model initial conditions are not observationally constrained. Our model results in a series of quasi-periodic SSEs that vary considerably over time. For example, the recurrence intervals range between one and 5 years (Text S3 in Supporting Information S1). Our approach neglects the (small) volumetric stress changes induced by slow slip outside the megathrust interface, which may lead to inconsistencies when extending the linked dynamic rupture models to include off-fault plasticity (Ma & Nie, 2019; Ulrich et al., 2022) in future work. Although inertia effects of slow slip are expected to be mostly minor, the complex long-term stress evolution and short-lived changes in stressing rate that we find here motivate future work, for example, using an integrated dynamic switch between inter- and co-seismic stages (e.g., Liu et al., 2020).

By coupling porosity and permeability evolution to elastic fault deformation, Yang and Dunham (2023) demonstrate the potentially critical role of pore fluid transportation and permeability evolution on slow slip and seismic cycles in a 2D antiplane fault model. Using a two-phase flow model that couples solid rock deformation and pervasive fluid flow, dal Zilio et al. (2020) investigate the effect of poroelastic coupling on long-term fault evolution in a solid-fluid constitutive framework but restricted to 2D. Focusing on the geodetically-constrained SSE source characteristics and for computational efficiency, we here omit potential SSE-underlying poroelastic effects (e.g., Heimisson et al., 2019). These can be caused, for example, by the dynamics of fluid migration and pressure variations within porous materials and will be important to study, specifically in 3D, in future work.

5. Conclusions

We construct a 3D dynamic rupture model of the 2014 Guerrero earthquake initiated solely by a geodetically constrained long-term model of the 2014 SSE and not by three preceding events. Our chosen frictional parameters balance slow slip transient stressing with depth-dependent fault strength and frictional strength drop, resulting in realistic co-seismic dynamics, especially when compared to alternative models with differing friction coefficients. Our mechanically self-consistent and data-driven 3D models of long-term SSE cycles, megathrust earthquake initiation, and rupture dynamics in the Guerrero Seismic Gap contribute to a better understanding of the earthquake generation process. They can potentially lead to improved time-dependent operational earthquake forecasting (Uchida & Bürgmann, 2021). By incorporating the transient stress evolution of slow-slip before co-seismic rupture and asperities in co-seismic friction drop, our models reproduce the kinematic and dynamic characteristics of both aseismic slip and co-seismic rupture and reveal their physical link. Although long-term

stress does not continuously accumulate, the accelerating migrating SSE fronts transiently increase shear stress at the down-dip end of the seismogenic portion of the megathrust. The SSE-induced transient stresses are not only large enough to nucleate megathrust earthquakes but also increase the complexity of 3D rupture dynamics. Improvements in the detection of transient aseismic slip deformation will aid in assessing seismic hazards in coastal regions (A. Kato et al., 2012; Socquet et al., 2017b). Furthermore, identifying distinct acceleration signals might be routinely possible in future regionally dense networks, specifically off-shore (Hilley et al., 2022).

Conflict of Interest

The authors declare no conflicts of interest relevant to this study.

Data Availability Statement

We use TriBIE (<https://github.com/daisy20170101/TriBIE>) for the slow slip simulation and SeisSol Master branch, available on GitHub (<https://github.com/SeisSol/SeisSol>) for 3D dynamic rupture simulation. Instructions for downloading, installing, and running the code are available in the SeisSol documentation at <https://seissol.readthedocs.io/>. Downloading and compiling instructions are at <https://seissol.readthedocs.io/en/latest/compiling-seissol.html>. Instructions for setting up and running simulations are at <https://seissol.readthedocs.io/en/latest/configuration.html>. Quickstart containerized installations and introductory materials are provided in the docker container and Jupyter notebooks at <https://github.com/SeisSol/Training>. Example problems and model configuration files are provided at <https://github.com/SeisSol/Examples>, many of which reproduce the SCEC 3D Dynamic Rupture benchmark problems described at https://strike.scec.org/cvws/benchmark_descriptions.html. The documentation of TriBIE can be found at <https://github.com/daisy20170101/TriBIE>. Community SEAS benchmark examples can be found at <https://strike.scec.org/cvws/cgi-bin/seas.cgi>. We use the software SKUA-GOCAD (pdgm.com/products/skua-gocad/) to produce all 3D fault models. The earthquake source data of the 2014 Guerro event is from USGS (<https://earthquake.usgs.gov/earthquakes/eventpage/usb00pq41/executive>) and GCMT (<https://www.globalcmt.org>). All input files and meshes required to reproduce the TriBIE long-term slow slip cycle and SeisSol earthquake dynamic rupture scenarios can be downloaded freely from Zenodo repository (<https://doi.org/10.5281/zenodo.6956697>).

Acknowledgments

We thank Editor Marcos Moreno, Eric Dunham, and two anonymous reviewers for their constructive comments. We thank Dmitry Garagash for useful discussions. This work was supported by the European Research Council (ERC) under the European Union's Horizon 2020 research and innovation programme (TEAR, Grant 852992). The authors acknowledge additional support by the National Science Foundation (Grants EAR-2121568, EAR-2222586, OAC-2311208, and OAC-2139536), the National Aeronautics and Space Administration (80NSSC20K0495), and Horizon Europe (ChEESE-2P Grant 101093038, DT-Geo Grant 101058129, and Geo-Inquire Grant 101058518). Computing resources were provided by the Leibniz Supercomputing Centre (LRZ, project No. pr63qo and No. pr49ha on SuperMUC-NG) and by the Institute of Geophysics of LMU Munich (Oeser et al., 2006). We thank Andrea Perez-Silva for a number of initial tests during her Master's thesis. We thank Dr. Mathilde Radiguet for kindly sharing the GPS inversion results of the Guerrero SSE. We appreciate the fruitful discussion with Dr. Yoshihiro Kaneko, Dr. Luis Dalguer, and the seismology group Ludwig-Maximilian-University of Munich (LMU). Open Access funding enabled and organized by Projekt DEAL.

References

Abercrombie, R. E. (2021). Resolution and uncertainties in estimates of earthquake stress drop and energy release. *Philosophical Transactions of the Royal Society A: Mathematical, Physical & Engineering Sciences*, 379(2196), 20200131. <https://doi.org/10.1098/rsta.2020.0131>

Abercrombie, R. E., & Rice, J. R. (2005). Can observations of earthquake scaling constrain slip weakening? *Geophysical Journal International*, 162(2), 406–424. <https://doi.org/10.1111/j.1365-246x.2005.02579.x>

Ampuero, J.-P., & Rubin, A. M. (2008). Earthquake nucleation on rate and state faults: Aging and slip laws. *Journal of Geophysical Research*, 113(B01302). <https://doi.org/10.1029/2007JB005082>

Andrews, D. J. (1985). Dynamic plane-strain shear rupture with a slip-weakening friction law calculated by a boundary integral method. *BSSA*, 75(1), 1–21. <https://doi.org/10.1785/BSSA0750010001>

Aochi, H., & Twardzik, C. (2020). Imaging of seismogenic asperities of the 2016 ML 6.0 Amatrice, Central Italy, earthquake through dynamic rupture simulations. *Pure and Applied Geophysics*, 177(5), 1931–1946. <https://doi.org/10.1007/s00024-019-02199-z>

Audet, P., Bostock, M. G., Christensen, N. I., & Peacock, S. M. (2009). Seismic evidence for overpressured subducted oceanic crust and megathrust fault sealing. *Nature*, 457(7225), 76–78. <https://doi.org/10.1038/nature07650>

Audet, P., & Bürgmann, R. (2014). Possible control of subduction zone slow-earthquake periodicity by silica enrichment. *Nature*, 510(7505), 389–393. <https://doi.org/10.1038/nature13391>

Beeler, N. M., Tullis, T. E., Blanpied, M. L., & Weeks, J. D. (1996). Frictional behavior of large displacement experimental faults. *Journal of Geophysical Research*, 101(B4), 8697–8715. <https://doi.org/10.1029/96jb00411>

Bilek, S. L., & Lay, T. (1999). Rigidity variations with depth along interplate megathrust faults in subduction zones. *Nature*, 400(6743), 443–446. <https://doi.org/10.1038/22739>

Bizzarri, A., & Cocco, M. (2003). Slip-weakening behavior during the propagation of dynamic ruptures obeying rate- and state-dependent friction laws. *Journal of Geophysical Research*, 108(B8). <https://doi.org/10.1029/2002jb002198>

Breuer, A., Heinecke, A., Rettenberger, S., Bader, M., Gabriel, A.-A., & Pelties, C. (2014). Sustained petascale performance of seismic simulations with SeisSol on SuperMUC. In *International supercomputing conference* (pp. 1–18).

Bürgmann, R. (2018). The geophysics, geology and mechanics of slow fault slip. *Earth and Planetary Science Letters*, 495, 112–134. <https://doi.org/10.1016/j.epsl.2018.04.062>

Byerlee, J. (1978). Friction of rocks [Book section]. In *Rock friction and earthquake prediction* (pp. 615–626). Springer.

Cattania, C. (2019). Complex earthquake sequences on simple faults. *Geophysical Research Letters*, 46(17–18), 10384–10393. <https://doi.org/10.1029/2019gl083628>

Cattania, C., & Segall, P. (2021). Precursory slow slip and foreshocks on rough faults. *Journal of Geophysical Research: Solid Earth*, 126(4), e2020JB020430. <https://doi.org/10.1029/2020JB020430>

Collettini, C., Tesei, T., Scuderi, M., Carpenter, B., & Viti, C. (2019). Beyond Byerlee friction, weak faults and implications for slip behavior. *Earth and Planetary Science Letters*, 519, 245–263. <https://doi.org/10.1016/j.epsl.2019.05.011>

dal Zilio, L., Lapusta, N., & Avouac, J. (2020). Unraveling scaling properties of slow-slip events. <https://doi.org/10.1029/2020GL087477>

Day, S. M., Dalguer, L. A., Lapusta, N., & Liu, Y. (2005). Comparison of finite difference and boundary integral solutions to three-dimensional spontaneous rupture. *Journal of Geophysical Research*, 110(B12). <https://doi.org/10.1029/2005jb003813>

DeMets, C., Gordon, R. G., & Argus, D. F. (2010). Geologically current plate motions. *Geophysical Journal International*, 181(1), 1–80. <https://doi.org/10.1111/j.1365-246X.2009.04491.x>

Dieterich, J. H. (1979). Modeling of rock friction 1. Experimental results and constitutive equations. *Journal of Geophysical Research*, 84(B5), 2161–2168. <https://doi.org/10.1029/JB084iB05p02161>

Di Toro, G., Goldsby, D. L., & Tullis, T. E. (2004). Friction falls towards zero in quartz rock as slip velocity approaches seismic rates. *Nature*, 427(6973), 436–439. <https://doi.org/10.1038/nature02249>

Di Toro, G., Han, R., Hirose, T., De Paola, N., Nielsen, S., Mizoguchi, K., et al. (2011). Fault lubrication during earthquakes. *Nature*, 471(7339), 494–498. <https://doi.org/10.1038/nature09838>

Dougherty, S. L., & Clayton, R. W. (2014). Seismicity and structure in central Mexico: Evidence for a possible slab tear in the South Cocos plate. *Journal of Geophysical Research*, 119(4), 3424–3447. <https://doi.org/10.1002/2013jb010883>

Douglas, A., Beavan, J., Wallace, L., & Townend, J. (2005). Slow slip on the northern Hikurangi subduction interface, New Zealand. *Geophysical Research Letters*, 32(L16305). <https://doi.org/10.1029/2005GL023607>

Dragert, H., Wang, K., & James, T. S. (2001). A silent slip event on the deeper Cascadia subduction interface. *Science*, 292(5521), 1525–1528. <https://doi.org/10.1126/science.1060152>

Dumbser, M., & Käser, M. (2006). An arbitrary high-order discontinuous Galerkin method for elastic waves on unstructured meshes—II. the three-dimensional isotropic case. *Geophysical Journal International*, 167(1), 319–336. <https://doi.org/10.1111/j.1365-246X.2006.03120.x>

Dziewonski, A. M., Chou, T.-A., & Woodhouse, J. H. (1981). Determination of earthquake source parameters from waveform data for studies of global and regional seismicity. *Journal of Geophysical Research*, 86(B4), 2825–2852. <https://doi.org/10.1029/JB086iB04p02825>

Ekström, G., Nettles, M., & Dziewonski, A. (2012). The global CMT project 2004–2010: Centroid-moment tensors for 13,017 earthquakes. *Physics of the Earth and Planetary Interiors*, 200, 1–9. <https://doi.org/10.1016/j.pepi.2012.04.002>

Erickson, B. A., Jiang, J., Lambert, V., Barbot, S. D., Abdelmeguid, M., Almqvist, M., et al. (2023). Incorporating full elastodynamic effects and dipping fault geometries in community code verification exercises for simulations of earthquake sequences and aseismic slip (seas). *Bulletin of the Seismological Society of America*, 113(2), 499–523. <https://doi.org/10.1785/0120220066>

Frank, W., Shapiro, N., Husker, A., Kostoglodov, V., Bhat, H., & Campillo, M. (2015). Along-fault pore-pressure evolution during a slow-slip event in Guerrero, Mexico. *Earth and Planetary Science Letters*, 413, 135–143. <https://doi.org/10.1016/j.epsl.2014.12.051>

Frank, W. B., Radiguet, M., Rousset, B., Shapiro, N. M., Husker, A. L., Kostoglodov, V., et al. (2015). Uncovering the geodetic signature of silent slip through repeating earthquakes. *Geophysical Research Letters*, 42(8), 2774–2779. <https://doi.org/10.1002/2015gl063685>

Gabriel, A.-A., Garagash, D. I., Palgunadi, K. H., & Mai, P. M. (2023). Fault-size dependent fracture energy explains multi-scale seismicity and cascading earthquakes. <https://doi.org/10.48550/arXiv.2307.15201>

Galis, M., Pelties, C., Kristek, J., Moczo, P., Ampuero, J.-P., & Mai, P. M. (2014). On the initiation of sustained slip-weakening ruptures by localized stresses. *Geophysical Journal International*, 200(2), 890–909. <https://doi.org/10.1093/gji/ggu436>

Galvez, P., Ampuero, J.-P., Dalguer, L. A., Somala, S. N., & Nissen-Meyer, T. (2014). Dynamic earthquake rupture modelled with an unstructured 3-D spectral element method applied to the 2011 M9 Tohoku earthquake. *Geophysical Journal International*, 198(2), 1222–1240. <https://doi.org/10.1093/gji/ggu203>

Galvez, P., Dalguer, L. A., Ampuero, J., & Giardini, D. (2016). Rupture reactivation during the 2011 MW 9.0 Tohoku earthquake: Dynamic rupture and ground-motion simulations/rupture reactivation during the 2011 MW 9.0 Tohoku earthquake: Dynamic rupture and ground-motion simulations. *Bulletin of the Seismological Society of America*, 106(3), 819–831. <https://doi.org/10.1785/0120150153>

Gao, X., & Wang, K. (2017). Rheological separation of the megathrust seismogenic zone and episodic tremor and slip. *Nature*, 543(7645), 416–419. <https://doi.org/10.1038/nature21389>

Garagash, D. I. (2021). Fracture mechanics of rate-and-state faults and fluid injection induced slip. *Philosophical Transactions of the Royal Society A*, 379(2196), 20200129. <https://doi.org/10.1098/rsta.2020.0129>

Gualandi, A., Perfettini, H., Radiguet, M., Cotte, N., & Kostoglodov, V. (2017). GPS deformation related to the M_W 7.3, 2014, Papaoa earthquake (Mexico) reveals the aseismic behavior of the Guerrero seismic gap. *Geophysical Research Letters*, 44(12), 6039–6047. <https://doi.org/10.1002/2017gl072913>

Guérin-Marthe, S., Nielsen, S., Bird, R., Giani, S., & Di Toro, G. (2019). Earthquake nucleation size: Evidence of loading rate dependence in laboratory faults. *Journal of Geophysical Research: Solid Earth*, 124(1), 689–708. <https://doi.org/10.1029/2018JB016803>

Harris, R. A., Barall, M., Aagaard, B. T., Ma, S., Daniel Roten, e. a., Olsen, K. B., et al. (2018). A suite of exercises for verifying dynamic earthquake rupture codes. *Seismological Research Letters*, 89(3), 1146–1162. <https://doi.org/10.1785/0220170222>

Harris, R. A., Barall, M., Lockner, D. A., Moore, D. E., Ponce, D. A., Graymer, R. W., et al. (2021). A geology and geodesy based model of dynamic earthquake rupture on the Rodgers Creek-Hayward-Calaveras fault system, California. *Journal of Geophysical Research: Solid Earth*, 126(3). <https://doi.org/10.1029/2020JB020577>

He, C., Wang, Z., & Yao, W. (2007). Frictional sliding of gabbro gouge under hydrothermal conditions. *Tectonophysics*, 445(3–4), 353–362. <https://doi.org/10.1016/j.tecto.2007.09.008>

Heimisson, E. R., Dunham, E. M., & Almqvist, M. (2019). Poroelastic effects destabilize mildly rate-strengthening friction to generate stable slow slip pulses. *Journal of the Mechanics and Physics of Solids*, 130, 262–279. <https://doi.org/10.1016/j.jmps.2019.06.007>

Heinecke, A., Breuer, A., Rettenberger, S., Bader, M., Gabriel, A., Pelties, C., et al. (2014). Petascale high order dynamic rupture earthquake simulations on heterogeneous supercomputers [Conference Proceedings]. In *Sc '14: Proceedings of the international conference for high performance computing* (pp. 3–14). Networking, Storage and Analysis. <https://doi.org/10.1109/SC.2014.6>

Hilley, G. E., Brodsky, E. E., Roman, D., Shillington, D. J., Brudzinski, M., Behn, M., et al. (2022). SZ4D implementation plan. *SZ4D*. <https://doi.org/10.25740/hy589fc7561>

Hirono, T., Tsuda, K., Tanikawa, W., Ampuero, J. P., Shibasaki, B., Kinoshita, M., & Mori, J. J. (2016). Near-trench slip potential of megquake evaluated from fault properties and conditions. *Scientific Reports*, 6(1), 28184. <https://doi.org/10.1038/srep28184>

Husker, A. L., Kostoglodov, V., Cruz-Atienza, V. M., Legrand, D., Shapiro, N. M., Payero, J. S., et al. (2012). Temporal variations of non-volcanic tremor (NVT) locations in the Mexican subduction zone: Finding the NVT sweet spot. *Geochemistry, Geophysics, Geosystems*, 13(3). <https://doi.org/10.1029/2011gc003916>

Ida, Y. (1972). Cohesive force across the tip of a longitudinal-shear crack and Griffith's specific surface energy. *Journal of Geophysical Research*, 77(20), 3796–3805. <https://doi.org/10.1029/jb077i020p03796>

Ide, S., & Aochi, H. (2005). Earthquakes as multiscale dynamic ruptures with heterogeneous fracture surface energy. *Journal of Geophysical Research*, 110(B11). <https://doi.org/10.1029/2004jb003591>

Jiang, J., Erickson, B. A., Lambert, V. R., Ampuero, J.-P., Ando, R., Barbot, S. D., et al. (2022). Community-driven code comparisons for three-dimensional dynamic modeling of sequences of earthquakes and aseismic slip. *Journal of Geophysical Research*, 127(3), e2021JB023519. <https://doi.org/10.1029/2021JB023519>

Kaneko, Y., Ampuero, J.-P., & Lapusta, N. (2011). Spectral-element simulations of long-term fault slip: Effect of low-rigidity layers on earthquake-cycle dynamics. *Journal of Geophysical Research*, 116(B10), B10313. <https://doi.org/10.1029/2011JB008395>

Kaneko, Y., Fukuyama, E., & Hamling, I. J. (2017). Slip-weakening distance and energy budget inferred from near-fault ground deformation during the 2016 MW7.8 Kaikoura earthquake. *Geophysical Research Letters*, 44(10), 4765–4773. <https://doi.org/10.1002/2017GL073681>

Kaneko, Y., Lapusta, N., & Ampuero, J. (2008). Spectral element modeling of spontaneous earthquake rupture on rate and state faults: Effect of velocity-strengthening friction at shallow depths. *Journal of Geophysical Research*, 113(B9). <https://doi.org/10.1029/2007JB005553>

Käser, M., & Dumbser, M. (2006). An arbitrary high-order discontinuous Galerkin method for elastic waves on unstructured meshes—I. The two-dimensional isotropic case with external source terms. *Geophysical Journal International*, 166(2), 855–877. <https://doi.org/10.1111/j.1365-246X.2006.03051.x>

Kato, A., Obara, K., Igarashi, T., Tsuruoka, H., Nakagawa, S., & Hirata, N. (2012). Propagation of slow slip leading up to the 2011 M_W 9.0 Tohoku-Oki earthquake. *Science*, 335(6069), 705–708. <https://doi.org/10.1126/science.1215141>

Kato, N. (2012). Fracture energies at the rupture nucleation points of large interplate earthquakes. *Earth and Planetary Science Letters*, 353–354, 190–197. <https://doi.org/10.1016/j.epsl.2012.08.015>

Khoshmanesh, M., Shirzaei, M., & Uchida, N. (2020). Deep slow-slip events promote seismicity in northeastern Japan megathrust. *Earth and Planetary Science Letters*, 540, 116261. <https://doi.org/10.1016/j.epsl.2020.116261>

Kim, Y., Clayton, R. W., & Jackson, J. M. (2010). Geometry and seismic properties of the subducting Cocos plate in central Mexico. *Journal of Geophysical Research: Solid Earth*, 115(B6). <https://doi.org/10.1029/2009JB006942>

Kostoglodov, V., Bandy, W., Dominguez, J., & Mena, M. (1996). Gravity and seismicity over the Guerrero seismic gap, Mexico. *Geophysical Research Letters*, 23(23), 3385–3388. <https://doi.org/10.1029/96gl03159>

Krenz, L., Uphoff, C., Ulrich, T., Gabriel, A.-A., Abrahams, L. S., Dunham, E. M., & Bader, M. (2021). 3D Acoustic-elastic coupling with gravity: The dynamics of the 2018 Palu, Sulawesi earthquake and tsunami. In *The international conference for high performance computing, networking, storage and analysis*. Association for Computing Machinery. <https://doi.org/10.1145/3458817.3476173>

Lapusta, N., & Liu, Y. (2009). Three-dimensional boundary integral modeling of spontaneous earthquake sequences and aseismic slip. *Journal of Geophysical Research*, 114(B09303). <https://doi.org/10.1029/2008JB005934>

Lay, T., Kanamori, H., Ammon, C. J., Koper, K. D., Hutko, A. R., Ye, L., et al. (2012). Depth-varying rupture properties of subduction zone megathrust faults. *Journal of Geophysical Research*, 117(B04311), B04311. <https://doi.org/10.1029/2011JB009133>

Li, D., & Liu, Y. (2016). Spatiotemporal evolution of slow slip events in a non-planar fault model for northern Cascadia subduction zone. *Journal of Geophysical Research: Solid Earth*, 63(3), 959–968. <https://doi.org/10.1002/2016JB012857>

Li, D., & Liu, Y. (2017). Modeling slow-slip segmentation in Cascadia subduction zone constrained by tremor locations and gravity anomalies. *Journal of Geophysical Research: Solid Earth*, 122(4), 3138–3157. <https://doi.org/10.1002/2016JB013778>

Li, T., & Rubin, A. M. (2017). A microscopic model of rate and state friction evolution. *Journal of Geophysical Research*, 122(8), 6431–6453. <https://doi.org/10.1002/2017JB013970>

Linde, A. T., Gladwin, M. T., Johnston, M. J., Gwyther, R. L., & Bilham, R. G. (1996). A slow earthquake sequence on the San Andreas fault. *Nature*, 383(6595), 65–68. <https://doi.org/10.1038/383065a0>

Liu, D., Duan, B., & Luo, B. (2020). EQsimu: A 3-D finite element dynamic earthquake simulator for multicycle dynamics of geometrically complex faults governed by rate- and state-dependent friction. *Geophysical Journal International*, 220(1), 598–609. <https://doi.org/10.1093/gji/gjz475>

Liu, Y., & Rice, J. R. (2007). Spontaneous and triggered aseismic deformation transients in a subduction fault model. *Journal of Geophysical Research*, 112(B9), B09404. <https://doi.org/10.1029/2007JB004930>

Liu, Y., & Rice, J. R. (2009). Slow slip predictions based on granite and gabbro friction data compared to GPS measurements in northern Cascadia. *Journal of Geophysical Research*, 114(B9), B09407. <https://doi.org/10.1029/2008JB006142>

Liu, Y., & Rubin, A. M. (2010). Role of fault gouge dilatancy on aseismic deformation transients. *Journal of Geophysical Research*, 115(B10414). <https://doi.org/10.1029/2010JB007522>

Liu, Y. J. (2013). Numerical simulations on megathrust rupture stabilized under strong dilatancy strengthening in slow slip region. *Geophysical Research Letters*, 40(7), 1311–1316. <https://doi.org/10.1002/grl.50298>

Lowry, A. R., Larson, K. M., Kostoglodov, V., & Bilham, R. (2001). Transient fault slip in Guerrero, southern Mexico. *Geophysical Research Letters*, 28(19), 3753–3756. <https://doi.org/10.1029/2001gl013238>

Ma, S., & Nie, S. (2019). Dynamic wedge failure and along-arc variations of tsunamigenesis in the Japan trench margin. *Geophysical Research Letters*, 46(15), 8782–8790. <https://doi.org/10.1029/2019GL083148>

Madden, E. H., Ulrich, T., & Gabriel, A.-A. (2022). The state of pore fluid pressure and 3-d megathrust earthquake dynamics. *Journal of Geophysical Research*, 127(4), e2021JB023382. <https://doi.org/10.1029/2021JB023382>

Manea, V. C., & Manea, M. (2011). Flat-slab thermal structure and evolution beneath central Mexico. *Pure and Applied Geophysics*, 168(8), 1475–1487. <https://doi.org/10.1007/s00024-010-0207-9>

Meng, Q., & Duan, B. (2022). Dynamic modeling of interactions between shallow slow-slip events and subduction earthquakes. *Seismological Research Letters*, 94(1), 206–216. <https://doi.org/10.1785/0220220138>

Noda, H., Dunham, E. M., & Rice, J. R. (2009). Earthquake ruptures with thermal weakening and the operation of major faults at low overall stress levels. *Journal of Geophysical Research*, 114(B07302). <https://doi.org/10.1029/2008JB006143>

Noda, H., Lapusta, N., & Kanamori, H. (2013). Comparison of average stress drop measures for ruptures with heterogeneous stress change and implications for earthquake physics. *Geophysical Journal International*, 193(3), 1691–1712. <https://doi.org/10.1093/gji/ggt074>

Obara, K., & Kato, A. (2016). Connecting slow earthquakes to huge earthquakes. *Science*, 353(6296), 253–257. <https://doi.org/10.1126/science.aaf1512>

Oeser, J., Bunge, H.-P., & Mohr, M. (2006). Cluster design in the earth sciences Tethys. In *International conference on high performance computing and communications* (pp. 31–40).

Oglesby, D. D., & Mai, P. M. (2012). Fault geometry, rupture dynamics and ground motion from potential earthquakes on the north Anatolian fault under the sea of Marmara. *Geophysical Journal International*, 188(3), 1071–1087. <https://doi.org/10.1111/j.1365-246X.2011.05289.x>

Palmer, A. C., & Rice, J. R. (1973). The growth of slip surfaces in the progressive failure of over-consolidated clay. *Proceedings of the Royal Society of London. A. Mathematical and Physical Sciences*, 332(1591), 527–548. <https://doi.org/10.1098/rspa.1973.0040>

Pelties, C., de la Puente, J., Ampuero, J.-P., Brietzke, G. B., & Käser, M. (2012). Three-dimensional dynamic rupture simulation with a high-order discontinuous Galerkin method on unstructured tetrahedral meshes. *Journal of Geophysical Research*, 117(B2). <https://doi.org/10.1029/2011JB008857>

Pelties, C., Gabriel, A. A., & Ampuero, J. P. (2014). Verification of an ADER-DG method for complex dynamic rupture problems. *Geoscientific Model Development*, 7(3), 847–866. <https://doi.org/10.5194/gmd-7-847-2014>

Peng, Z., & Gomberg, J. (2010). An integrated perspective of the continuum between earthquakes and slow-slip phenomena. *Nature Geoscience*, 3(9), 599–607. <https://doi.org/10.1038/ngeo940>

Pérez-Campos, X., Kim, Y., Husker, A., Davis, P. M., Clayton, R. W., Iglesias, A., et al. (2008). Horizontal subduction and truncation of the Cocos plate beneath central Mexico. *Geophysical Research Letters*, 35(18). <https://doi.org/10.1029/2008GL035127>

Perez-Silva, A., Li, D., Gabriel, A.-A., & Kaneko, Y. (2021). 3D modeling of long-term slow slip events along the flat-slab segment in the Guerrero seismic gap, Mexico. *Geophysical Research Letters*, 48(13), e2021GL092968. <https://doi.org/10.1029/2021GL092968>

Perry, S. M., Lambert, V., & Lapusta, N. (2020). Nearly magnitude-invariant stress drops in simulated crack-like earthquake sequences on rate-and-state faults with thermal pressurization of pore fluids. *Journal of Geophysical Research*, 125(3), e2019JB018597. <https://doi.org/10.1029/2019JB018597>

Plata-Martinez, R., Ide, S., Shinohara, M., Garcia, E. S., Mizuno, N., Dominguez, L. A., et al. (2021). Shallow slow earthquakes to decipher future catastrophic earthquakes in the Guerrero seismic gap. *Nature Communications*, 12(1), 3976. <https://doi.org/10.1038/s41467-021-24210-9>

Pritchard, M. E., Allen, R. M., Becker, T. W., Behn, M. D., Brodsky, E. E., Bürgmann, R., et al. (2020). New opportunities to study earthquake precursors. *Seismological Research Letters*, 91(5), 2444–2447. <https://doi.org/10.1785/0220200089>

Radiguet, M., Cotton, F., Vergnolle, M., Campillo, M., Walpersdorf, A., Cotte, N., & Kostoglodov, V. (2012). Slow slip events and strain accumulation in the guerrero gap, Mexico. *Journal of Geophysical Research*, 117(B4). <https://doi.org/10.1029/2011JB008801>

Radiguet, M., Perfettini, H., Cotte, N., Gualandi, A., Valette, B., Kostoglodov, V., et al. (2016). Triggering of the 2014 MW7.3 Papanoa earthquake by a slow slip event in Guerrero, Mexico. *Nature Geoscience*, 9(11), 829–833. <https://doi.org/10.1038/ngeo2817>

Ramos, M. D., & Huang, Y. (2019). How the transition region along the Cascadia megathrust influences Coseismic behavior: Insights from 2-D dynamic rupture simulations. *Geophysical Research Letters*, 46(4), 1973–1983. <https://doi.org/10.1029/2018gl080812>

Ramos, M. D., Huang, Y., Ulrich, T., Li, D., Gabriel, A.-A., & Thomas, A. M. (2021). Assessing margin-wide rupture behaviors along the Cascadia megathrust with 3-D dynamic rupture simulations. *Journal of Geophysical Research*, 126(7), e2021JB022005. <https://doi.org/10.1029/2021JB022005>

Rettenberger, S., Meister, O., Bader, M., & Gabriel, A.-A. (2016). Asagi: A parallel server for adaptive geoinformation. In *Proceedings of the exascale applications and software conference 2016*. Association for Computing Machinery. <https://doi.org/10.1145/2938615.2938618>

Rice, J. R. (1993). Spatiotemporal complexity of slip on a fault. *Journal of Geophysical Research*, 98(B6), 9885–9907. <https://doi.org/10.1029/93JB00191>

Rice, J. R., & Ben-Zion, Y. (1996). Slip complexity in earthquake fault models. *Proceedings of the National Academy of Sciences*, 93(9), 3811–3818. <https://doi.org/10.1073/pnas.93.9.3811>

Rousset, B., Bürgmann, R., & Campillo, M. (2019). Slow slip events in the roots of the San Andreas fault. *Science Advances*, 5(2), eaav3274. <https://doi.org/10.1126/sciadv.aav3274>

Rubin, A. M., & Ampuero, J.-P. (2005). Earthquake nucleation on (Aigne) rate and state faults. *Journal of Geophysical Research*, 110(B11312). <https://doi.org/10.1029/2005JB003686>

Ruina, A. L. (1983). Slip instability and state variable friction laws. *Journal of Geophysical Research*, 88(B12), 10359–10370. <https://doi.org/10.1029/JB088B12p10359>

Ruiz, S., Metois, M., Fuenzalida, A., Ruiz, J., Leyton, F., Grandin, R., et al. (2014). Intense foreshocks and a slow slip event preceded the 2014 Iquique M_w 8.1 earthquake. *Science*, 345(6201), 1165–1169. <https://doi.org/10.1126/science.1256074>

Saffer, D. M., & Wallace, L. M. (2015). The frictional, hydrologic, metamorphic and thermal habitat of shallow slow earthquakes. *Nature Geoscience*, 8(8), 594–600. <https://doi.org/10.1038/ngeo2490>

Schwartz, S. Y., & Rokosky, J. M. (2007). Slow slip events and seismic tremor at Circum-Pacific subduction zones. *Reviews of Geophysics*, 45(3). <https://doi.org/10.1029/2006RG000208>

Segall, P., Rubin, A. M., Bradley, M., & Rice, J. R. (2010). Dilatant strengthening as a mechanism for slow slip events. *Journal of Geophysical Research*, 115(B12305), 115. <https://doi.org/10.1029/2010JB007449>

Shelly, D. R., Beroza, G. C., & Ide, S. (2007). Non-volcanic tremor and low-frequency earthquake swarms. *Nature*, 446(7133), 305–307. <https://doi.org/10.1038/nature05666>

Shelly, D. R., Beroza, G. C., Ide, S., & Nakamura, S. (2006). Low-frequency earthquakes in Shikoku, Japan, and their relationship to episodic tremor and slip. *Nature*, 442(7099), 188–191. <https://doi.org/10.1038/nature04931>

Socquet, A., Valdes, J. P., Jara, J., Cotton, F., Walpersdorf, A., Cotte, N., et al. (2017a). An 8 month slow slip event triggers progressive nucleation of the 2014 Chile megathrust. *Geophysical Research Letters*, 44(9), 4046–4053. <https://doi.org/10.1002/2017GL073023>

Socquet, A., Valdes, J. P., Jara, J., Cotton, F., Walpersdorf, A., Cotte, N., et al. (2017b). An 8 month slow slip event triggers progressive nucleation of the 2014 Chile megathrust. *Geophysical Research Letters*, 44(9), 4046–4053. <https://doi.org/10.1002/2017GL073023>

Song, T. R., Helmberger, D. V., Brudzinski, M. R., Clayton, R. W., Davis, P., Perez-Campos, X., & Singh, S. K. (2009). Subducting slab ultra-slow velocity layer coincident with silent earthquakes in southern Mexico. *Science*, 324(5926), 502–506. <https://doi.org/10.1126/science.1167595>

Stuart, W. D., Hildenbrand, T. G., & Simpson, R. W. (1997). Stressing of the New Madrid Seismic Zone by a lower crust detachment fault. *Journal of Geophysical Research*, 102(B12), 27623–27633. <https://doi.org/10.1029/97jb02716>

Thomas, M. Y., Lapusta, N., Noda, H., & Avouac, J.-P. (2014). Quasi-dynamic versus fully dynamic simulations of earthquakes and aseismic slip with and without enhanced Coseismic weakening. *Journal of Geophysical Research: Solid Earth*, 119(3), 1986–2004. <https://doi.org/10.1002/2013JB010615>

Tinti, E., Spudich, P., & Cocco, M. (2005). Earthquake fracture energy inferred from kinematic rupture models on extended faults. *Journal of Geophysical Research*, 110(B12). <https://doi.org/10.1029/2005jb003644>

Tobin, H. J., & Saffer, D. M. (2009). Elevated fluid pressure and extreme mechanical weakness of a plate boundary thrust, Nankai trough subduction zone. *Geology*, 37(8), 679–682. <https://doi.org/10.1130/g25752a.1>

Uchida, N., & Bürgmann, R. (2021). A decade of lessons learned from the 2011 tohoku-oki earthquake. *Reviews of Geophysics*, 59(2). <https://doi.org/10.1029/2020RG000713>

Uchida, N., Inuma, T., Nadeau, R. M., Bürgmann, R., & Hino, R. (2016). Periodic slow slip triggers megathrust zone earthquakes in northeastern Japan. *Science*, 351(6272), 488–492. <https://doi.org/10.1126/science.aad3108>

Uenishi, K., & Rice, J. R. (2003). Universal nucleation length for slip-weakening rupture instability under nonuniform fault loading. *Journal of Geophysical Research*, 108(B1). <https://doi.org/10.1029/2001jb001681>

Ulrich, T., Gabriel, A.-A., & Madden, E. H. (2022). Stress, rigidity and sediment strength control megathrust earthquake and tsunami dynamics. *Nature Geoscience*, 15(1), 67–73. <https://doi.org/10.1038/s41561-021-00863-5>

Uphoff, C., May, D. A., & Gabriel, A.-A. (2023). A discontinuous galerkin method for sequences of earthquakes and aseismic slip on multiple faults using unstructured curvilinear grids. *Geophysical Journal International*, 233(1), 586–626. <https://doi.org/10.1093/gji/gjac467>

Uphoff, C., Rettenberger, S., Bader, M., Madden, E. H., Ulrich, T., Wollherr, S., & Gabriel, A.-A. (2017). Extreme scale multi-physics simulations of the Tsunamigenic 2004 Sumatra megathrust earthquake. [Conference Paper]. <https://doi.org/10.1145/3126908.3126948>

Vallee, M., Charléty, J., Ferreira, A. M. G., Delouis, B., & Vergoz, J. (2011). SCARDEC: A new technique for the rapid determination of seismic moment magnitude, focal mechanism and source time functions for large earthquakes using body-wave deconvolution. *Geophysical Journal International*, 184(1), 338–358. <https://doi.org/10.1111/j.1365-246X.2010.04836.x>

van Zelst, I., Wollherr, S., Gabriel, A.-A., Madden, E. H., & van Dinther, Y. (2019). Modeling megathrust earthquakes across scales: One-way coupling from geodynamics and seismic cycles to dynamic rupture. *Journal of Geophysical Research: Solid Earth*, 124(11), 11414–11446. <https://doi.org/10.1029/2019JB017539>

Walton, M. A., Staisch, L. M., Dura, T., Pearl, J. K., Sherrod, B., Gomberg, J., et al. (2021). Toward an integrative geological and geophysical view of Cascadia subduction zone earthquakes. *Annual Review of Earth and Planetary Sciences*, 49(1), 367–398. <https://doi.org/10.1146/annurev-earth-071620-065605>

Wang, K. (2010). Finding fault in fault zones. *Science*, 329(5988), 152–153. <https://doi.org/10.1126/science.1192223>

Yang, Y., & Dunham, E. M. (2023). Influence of creep compaction and dilatancy on earthquake sequences and slow slip. *Journal of Geophysical Research*, 128(4), e2022JB025969. <https://doi.org/10.1029/2022JB025969>

Ye, L., Lay, T., Kanamori, H., & Rivera, L. (2016). Rupture characteristics of major and great ($mw \leq 7.0$) megathrust earthquakes from 1990 to 2015: 2.depth dependence. *Journal of Geophysical Research*, 121(2), 845–863. <https://doi.org/10.1002/2015jb012427>

Zhu, W., Allison, K. L., Dunham, E. M., & Yang, Y. (2020). Fault valving and pore pressure evolution in simulations of earthquake sequences and aseismic slip. *Nature Communications*, 11(1), 4833. <https://doi.org/10.1038/s41467-020-18598-z>

References From the Supporting Information

Aagaard, B. T., Knepley, M. G., & Williams, C. A. (2013). A domain decomposition approach to implementing fault slip in finite-element models of quasi-static and dynamic crustal deformation. *Journal of Geophysical Research*, 118(6), 3059–3079. <https://doi.org/10.1002/jgrb.50217>

Aniko Wirp, S., Gabriel, A.-A., Schmeller, M., Madden, E. H., van Zelst, I., Krenz, L., et al. (2021). 3d linked subduction, dynamic rupture, tsunami, and inundation modeling: Dynamic effects of supershear and tsunami earthquakes, hypocenter location, and shallow fault slip. *Frontiers in Earth Science*, 9. <https://doi.org/10.3389/feart.2021.626844>

Day, S. M. (1982). Three-dimensional simulation of spontaneous rupture: The effect of nonuniform prestress. *Bulletin of the Seismological Society of America*, 72(6A), 1881–1902.

Gabriel, A.-A., Ampuero, J.-P., Dalguer, L. A., & Mai, P. M. (2012). The transition of dynamic rupture styles in elastic media under velocity-weakening friction. *Journal of Geophysical Research*, 117(B9). <https://doi.org/10.1029/2012JB009468>

Kaneko, Y., Avouac, J., & Lapusta, N. (2010). Towards inferring earthquake patterns from geodetic observations of interseismic coupling. *Nature Geoscience*, 3(5), 363–369. <https://doi.org/10.1038/NGEO843>

Madden, E., Bader, M., Behrens, J., van Dinther, Y., Gabriel, A.-A., Rannabauer, L., et al. (2020). Linked 3D modeling of megathrust earthquake-tsunami events: From subduction to tsunami run up. *Geophysical Journal International*, 224(1), 487–516. <https://doi.org/10.1093/gji/ggaa484>

Marone, C. (1998). Laboratory-derived friction laws and their application to seismic faulting. *Annual Review of Earth and Planetary Sciences*, 26(1), 643–696. <https://doi.org/10.1146/annurev.earth.26.1.643>

Mikumo, T., Olsen, K. B., Fukuyama, E., & Yagi, Y. (2003). Stress-breakdown time and slip-weakening distance inferred from slip-velocity functions on earthquake faults. *Bulletin of the Seismological Society of America*, 93(1), 264–282. <https://doi.org/10.1785/0120020082>

Nuyen, C. P., & Schmidt, D. A. (2021). Filling the gap in Cascadia: The emergence of low-amplitude long-term slow slip. *Geochemistry, Geophysics, Geosystems*, 22(3), e2020GC009477. <https://doi.org/10.1029/2020GC009477>

Tinti, E., Casarotti, E., Ulrich, T., Taufiqurrahman, T., Li, D., & Gabriel, A.-A. (2021). Constraining families of dynamic models using geological, geodetic and strong ground motion data: The mw 6.5, October 30th, 2016, Norcia earthquake, Italy. *Earth and Planetary Science Letters*, 576, 117237. <https://doi.org/10.1016/j.epsl.2021.117237>

Wollherr, S., Gabriel, A.-A., & Mai, P. M. (2019). Landers 1992 “reloaded”: Integrative dynamic earthquake rupture modeling. *Journal of Geophysical Research*, 124(7), 6666–6702. <https://doi.org/10.1029/2018JB016355>

Wollherr, S., Gabriel, A.-A., & Uphoff, C. (2018). Off-fault plasticity in three-dimensional dynamic rupture simulations using a modal discontinuous Galerkin method on unstructured meshes: Implementation, verification and application. *Geophysical Journal International*, 214(3), 1556–1584. <https://doi.org/10.1093/gji/ggy213>